



**HAL**  
open science

# Rapid Gas Bubble Growth in Basaltic Magma as a Source of Deep Long Period Volcanic Earthquakes

Oleg Melnik, Vladimir Lyakhovsky, Nikolai Shapiro

► **To cite this version:**

Oleg Melnik, Vladimir Lyakhovsky, Nikolai Shapiro. Rapid Gas Bubble Growth in Basaltic Magma as a Source of Deep Long Period Volcanic Earthquakes. *Journal of Geophysical Research: Solid Earth*, 2024, 129 (11), 10.1029/2024JB029602 . hal-04788104

**HAL Id: hal-04788104**

**<https://hal.science/hal-04788104v1>**

Submitted on 19 Nov 2024

**HAL** is a multi-disciplinary open access archive for the deposit and dissemination of scientific research documents, whether they are published or not. The documents may come from teaching and research institutions in France or abroad, or from public or private research centers.

L'archive ouverte pluridisciplinaire **HAL**, est destinée au dépôt et à la diffusion de documents scientifiques de niveau recherche, publiés ou non, émanant des établissements d'enseignement et de recherche français ou étrangers, des laboratoires publics ou privés.






Distributed under a Creative Commons Attribution - NonCommercial - NoDerivatives 4.0 International License

# JGR Solid Earth

## RESEARCH ARTICLE

10.1029/2024JB029602

# Rapid Gas Bubble Growth in Basaltic Magma as a Source of Deep Long Period Volcanic Earthquakes

Oleg Melnik<sup>1</sup> , Vladimir Lyakhovsky<sup>2</sup> , and Nikolai M. Shapiro<sup>1</sup> 

<sup>1</sup>ISTerre, Université Grenoble Alpes, CNRS, Université Savoie Mont Blanc, IRD, Université Gustave Eiffel, Grenoble, France, <sup>2</sup>Geological Survey of Israel, Jerusalem, Israel

### Key Points:

- Spontaneous bubble nucleation leads to rapid pressure increase in a batch of magma
- Bubble nucleation in the center of a sill filled with magma results in a propagation of a nucleation front inside the sill
- Expanding sill generate P and S seismic waves with amplitudes and frequencies close to the observations

### Correspondence to:

N. M. Shapiro,  
Nikolai.Shapiro@univ-grenoble-alpes.fr

### Citation:

Melnik, O., Lyakhovsky, V., & Shapiro, N. M. (2024). Rapid gas bubble growth in basaltic magma as a source of Deep Long Period volcanic earthquakes. *Journal of Geophysical Research: Solid Earth*, 129, e2024JB029602. <https://doi.org/10.1029/2024JB029602>

Received 27 MAY 2024

Accepted 11 NOV 2024

### Author Contributions:

**Conceptualization:** Oleg Melnik, Vladimir Lyakhovsky, Nikolai M. Shapiro  
**Formal analysis:** Oleg Melnik, Vladimir Lyakhovsky, Nikolai M. Shapiro  
**Funding acquisition:** Nikolai M. Shapiro  
**Investigation:** Oleg Melnik, Vladimir Lyakhovsky, Nikolai M. Shapiro  
**Methodology:** Oleg Melnik, Vladimir Lyakhovsky  
**Software:** Oleg Melnik, Vladimir Lyakhovsky  
**Validation:** Oleg Melnik, Vladimir Lyakhovsky, Nikolai M. Shapiro  
**Visualization:** Vladimir Lyakhovsky, Nikolai M. Shapiro  
**Writing – original draft:** Oleg Melnik, Vladimir Lyakhovsky, Nikolai M. Shapiro

© 2024. The Author(s).

This is an open access article under the terms of the [Creative Commons Attribution-NonCommercial-NoDerivs License](https://creativecommons.org/licenses/by/4.0/), which permits use and distribution in any medium, provided the original work is properly cited, the use is non-commercial and no modifications or adaptations are made.

**Abstract** In this paper, we present numerical modeling aimed to explain Deep Long Period (DLP) events occurring in middle-to-lower crust beneath volcanoes and often observed in association with volcanic eruptions or their precursors. We consider a DLP generating mechanism caused by the rapid growth of gas bubbles in response to the slow decompression of H<sub>2</sub>O–CO<sub>2</sub> over-saturated basaltic magma. The nucleation and rapid growth of gas bubbles lead to rapid pressure change in the magma and elastic rebound of the host rocks, radiating seismic waves recorded as DLP events. The magma and host rocks are modeled as Maxwell bodies with different relaxation times and elastic moduli. Simulations of a single sill-shaped intrusion with different parameters demonstrate that realistic amplitudes and frequencies of P and S seismic waves can be obtained when considering intrusions with linear sizes of the order of 100 m. We then consider a case of two closely located sills and model their interaction. We speculate on conditions that can result in consecutive triggering of the bubble growth in multiple closely located batches of magma, leading to the generation of earthquake swarms or seismic tremors.

**Plain Language Summary** Volcano seismology is one of the main geophysical methods used to study volcanic processes and to forecast the eruptions. It is based on analysis of ground motion recorded by seismographs installed in the vicinity of volcanoes. Different seismic signals such as impulsive volcanic earthquakes and nearly continuous volcanic tremors are recorded during periods corresponding to preparation of eruptions. Some of them originate from depths of a few tens of kilometers, that is, from the roots of the system that feeds the magma supply to volcanoes and their eruptions. Therefore, such deep seismic sources are particularly interesting because they may represent early eruption precursors. While we still lack physical understanding of the processes leading to this deep volcanic seismicity, there are several reasons to consider that it is not caused by a sudden slip on faults responsible for the majority of “regular tectonic” earthquakes. In this paper, we use numerical simulations to test another possible mechanism of generation of deep volcanic earthquakes. Namely, we assume that they can be caused by rapid growth of bubbles from the gas that was initially dissolved in the magma. We use numerical simulations to demonstrate that this model predicts main properties of the observed seismic signals.

## 1. Introduction

Gas exsolution in the magma is one of the main driving forces behind the volcanic activity. The separation of gas and melt phases leads to the formation of bubbles, whose presence increases the magma buoyancy thereby leading to its ascent. Degassing is very strong at the very top part of volcanic systems where most of gases, especially H<sub>2</sub>O, no longer remain dissolved due to the pressure decrease (e.g., Wallace et al., 2015). Therefore, dynamics of gas bubbles in the magma is predominant during the eruptions (e.g., Cassidy et al., 2018; Jaupart & Vergnolle, 1988) and other near-surface volcano-related processes. In particular, the gas exsolution and associated bubble growth can cause significant magma pressure variations. If these pressure perturbations are sufficiently rapid, they are transmitted into the surrounding elastic media as seismic waves that can be recorded by seismographs as volcanic earthquakes. Such rapid pressure changes can occur when a magma volume first reaches the saturation level and then achieves the critical supersaturation after which the gas bubbles nucleate and grow rapidly (Lensky et al., 2006; Lyakhovsky et al., 1996).

In one scenario, a rapid decompression of a shallow intrusion caused by a sudden gas escape via conduit results in a critical magma supersaturation. This pressure drop is followed by a pressure recovery because of the gas bubble grows (Nishimura, 2004). B. Chouet et al. (2006) modeled such sequence of magma depressurization-

pressurization and related elastic deformation of the surrounding rocks in order to explain very long period seismic signals associated with the Vulcanian explosions at Popocatepetl Volcano in Mexico (B. Chouet et al., 2005). They considered a sill-shaped volume of rhyolitic magma at a depth of 1.5 km. The system response has been found to depend strongly on various parameters such as volatile diffusivity in the melt, the bubble number density, the initial bubble radius, and the shape of the intrusion. The model could reasonably explain observed seismic waveforms within the range of acceptable parameters and predicted pressure variations of the order of a few MPa with characteristic timescale of tens of seconds.

Another scenario has been recently considered by O. Melnik et al. (2020) to explain the Deep Long Period (DLP) earthquakes occurring in middle-to-lower crust beneath volcanoes and often associated with eruptions or their precursors (e.g., Aso & Tsai, 2014; Aso et al., 2013; Greenfield et al., 2022; Hensch et al., 2019; Ikegaya & Yamamoto, 2021; Kurihara & Obara, 2021; Kurihara et al., 2019; Lu & Bostock, 2022; Nichols et al., 2011; Pitt & Hill, 1994; Power et al., 2004; Shapiro, Droznin, et al., 2017; Song et al., 2023; Ukawa & Ohtake, 1987; Wech et al., 2020; White et al., 1996). In some cases, the origin of these DLP earthquakes has been attributed to the processes occurring within a cooling magma body stalled beneath the crust such thermal stresses (Aso et al., 2013) or “second boiling,” that is, repeated pressurization by volatiles exsolution during magma crystallization (Wech et al., 2020). However, such cooling-related mechanisms are unlikely for DLP events occurring beneath active volcanoes in association with eruptions. Previous studies of moment-tensor inversion of the DLP earthquakes (e.g., Aso & Ide, 2014; Hensch et al., 2019; Ikegaya & Yamamoto, 2021; Nakamichi et al., 2003) demonstrated a strong volumetric component in the seismic source suggesting a generating process involving pressure variations in a molten magma. Therefore, O. Melnik et al. (2020) suggested a possible DLP generating mechanism related to the rapid growth of gas bubbles in response to the slow decompression of over-saturated magma. In this model, a volume of magma saturated with H<sub>2</sub>O–CO<sub>2</sub> volatiles is slowly rising up which causes its depressurization. This magma first reaches the saturation level and then achieves the critical supersaturation after which gas bubbles nucleation causes rapid pressure and elastic stress variations resulting in seismic waves recorded as DLP earthquakes.

The model of O. Melnik et al. (2020) was particularly aimed to explain the DLP earthquakes occurring beneath the Klyuchevskoy volcano in Kamchatka, Russia (e.g., Fedotov et al., 2010; Koulakov et al., 2020; Shapiro, Sens-Schönfelder, et al., 2017) just beneath the crust-mantle boundary (Galina et al., 2020; Journeau et al., 2022; Levin et al., 2014; Shapiro, Droznin, et al., 2017) at a depth of approximately 30–35 km. A recent study of DLP earthquakes in this region (Galina & Shapiro, 2024) have shown that source mechanisms with dominating shear faulting (double couple) are unlikely to explain observations and that the observed signal amplitudes can be better predicted with mechanisms containing strong volumetric or single force components. In particular, expansion of sill-shaped magmatic intrusions has been found among the processes reasonably compatible with observations.

Recent studies suggested that primary Klyuchevskoy magma may contain more than 4 wt% H<sub>2</sub>O and 0.35–0.9 wt% CO<sub>2</sub> (Mironov & Portnyagin, 2011; Portnyagin et al., 2007, 2019). Single H<sub>2</sub>O volatile phase would result in a small saturation depth, but the addition of ~0.6 wt% of CO<sub>2</sub> decreases volatile solubility dramatically (e.g., Burgisser et al., 2015b; Papale, 1999) so that magma becomes super-saturated at pressures above 800 MPa (~30 km depth). This could imply that in the Klyuchevskoi magmas the gas bubbles start to appear at depths of 30–40 km. O. Melnik et al. (2020) verified this possibility of the deep gas exsolution with the “D-Compress” software (Burgisser et al., 2015a) and estimated the volatile solubility at depths close to 30 km in magmas containing 0.6–0.7 wt% and 3–5 wt% H<sub>2</sub>O. More recently developed “VESIcal” model (Iacovino et al., 2021) calibrated on experimental data sets at pressures up to 1 GPa (Wieser et al., 2022) showed the ranges of volatile content comparable to previously predicted by “D-Compress.” These computations have shown that the Klyuchevskoy magmas may become supersaturated at such large pressures and depths leading to bubble nucleation and rapid growth. The fluid in the bubble after nucleation contains 60–65 wt% CO<sub>2</sub> and 40–35 wt% H<sub>2</sub>O. At 800 MPa pressure and temperature of 1200 C, this fluid is supercritical and has a density of 900 kg/m<sup>3</sup>.

O. Melnik et al. (2020) have shown that for realistic magma compositions and values of the gas and bubble content, the elastic deformation of surrounding rocks forced by the expanding bubbly magma can be fast enough to generate seismic waves. They approximately estimated a volume of bubbly magma of ~10<sup>3</sup>–10<sup>4</sup>m<sup>3</sup> would be necessary to explain amplitudes of signals recorded from the DLP earthquakes beneath the Klyuchevskoy volcano. Nevertheless, this model contained important approximations. First, an instantaneous bubble nucleation in the whole batch of magma was assumed, similar to B. Chouet et al. (2006). However, such scenario is unlikely

within the slowly uplifting magma batch. In this case, we can rather expect that the bubble growth will be first triggered in a small volume and then the nucleation front will spontaneously propagate through the rest of the magma body. Second limitation of O. Melnik et al. (2020) was that only a spherical-shape intrusion was modeled. Also, excitation of seismic waves was not explicitly computed and the amplitudes of seismograms were predicted based on a simplified approximation.

To overcome the mentioned shortcomings, we developed a more complete and accurate model of generation of seismic waves by the pressure variations caused by bubbles growth in basaltic magma. The model is based on an accurate numerical solution of coupled fluid-elastic equations and includes: (a) a bubble nucleation occurring in the portion of the magma, where the pressure decreases below the saturation by a small threshold value; (b) a sill-shape magma intrusion, and (c) an exact estimation of the associated seismic potency (moment) tensor in order to compute the seismograms.

We start with formulating the mechanical model in Section 2. A particular attention is paid to an accurate description of the compressibility of the bubbly magma and its variations in association with the bubble growth. We then apply the developed mechanical framework to model the gas bubble growth in an intrusion shaped as a horizontal sill. The numerical implementation and model settings are described in Section 3. The results of the modeling are presented in Section 4 and their implications are discussed in Section 5. In particular, after considering solutions for a single sill-shaped intrusion with different parameters, we introduce a case of two closely located sills and model their interaction. We then speculate how such interaction can result in consecutive triggering of the bubble growth in multiple closely located intrusions and lead to generation of earthquake swarms or seismic tremors.

## 2. Mechanical Model of a DLP Earthquake Source

All variables and notations are summarized in Table 1.

### 2.1. Conceptual Model

We consider a scenario illustrated in Figure 1a. Basaltic magmas rising from the mantle are underplated beneath the Moho forming sill-shaped intrusions. Following O. Melnik et al. (2020), we consider that  $H_2O$ – $CO_2$  rich basaltic magma becomes oversaturated at these depths leading to a spontaneous nucleation and rapid growth of gas bubbles within the sill. This results in pressure variations coupled to elastic deformation of the surrounding rocks and generation of seismic waves that are then recorded by seismographs installed at the surface.

Evolution of the magma pressure in a small volume is schematically illustrated in Figure 1b. The slowly rising magma at some depth reaches the saturation pressure  $P_S$  and then becomes oversaturated. The spontaneous bubble nucleation does not start immediately at this saturation threshold but at some lower critical pressure  $P_0$ , that is, at a smaller depth where the sill is located.

In our study we focus on the processes of rapid deformation caused by the bubble growth and do not model the slow process of magma raising and gas diffusion prior the bubble nucleation. We start our simulation with considering a sill with initial homogeneous pressure  $P_{in}$  that is slightly above  $P_0$ :

$$P_{in} = P_0 + \delta P \quad (1)$$

This small “nucleation threshold”  $\delta P$  is introduced to avoid the simultaneous bubble growth in the whole magma volume. We then trigger the gas exsolution in an initial small volume (Figure 1c) by decreasing its pressure to  $P_0$ .

As argued in O. Melnik et al. (2020) (Methods section), the combined heterogeneous and homogeneous nucleation of bubbles in a small volume takes less than 0.01 s, that is, two orders of magnitude below typical bubble growth times. Therefore, we approximate the nucleation as an instantaneous process. The initial gas pressure  $P_g$  within the nucleating bubbles is equal to saturation threshold  $P_S$  (Lyakhovskiy et al., 1996) which is above the pressure in the surrounding melt  $P_0$ . As a result, the bubbles start to grow rapidly while their pressure initially decreases. The overall magma pressure  $P(t)$  grows rapidly and reaches some equilibrium level  $P_{eq}$ . Rapid pressure variations within this initial volume lead to perturbations of the pressure and elastic stresses in its vicinity and, in particular, to the pressure reduction in some parts of the sill. When this reduction reaches the nucleation threshold ( $P_0 = P_{in} - \delta P$ ), new bubbles nucleate and start to grow. Such “nucleation front” propagates along the whole

**Table 1**  
Notations and Variables

Notation	Variable description
$t$	Time
$t_n$	Time since bubble nucleation
$x$	Spatial cartesian coordinates
$u$	Displacement
$\epsilon^t$	Total strain
$\epsilon^e$	Elastic strain
$\epsilon^{irr}$	Irreversible strain
$\epsilon_v$	Volumetric strain
$\sigma$	Stress
$\tau$	Deviatoric stress
$P_m$	Pressure of the melt
$P_g$	Pressure of the gas
$P_b$	Pressure of the bubbly magma
$P_S$	Saturation pressure
$P_0$	Bubble nucleation pressure
$\Delta P$	Pressure over-saturation
$P_{in}$	Initial pressure
$\delta P$	Initial “threshold” above nucleation pressure
$P_{eq}$	Equilibrium pressure at the end of the bubble growth
$\rho$	Density
$\rho_g$	Gas density
$\rho_m$	Melt density
$\lambda_s, \mu_s$	Lame elastic moduli of the solid
$\lambda_m$	Shear modulus of the melt
$K_m$	Bulk modulus of the melt
$\eta$	Viscosity of the melt
$R$	Radius of a gas bubble
$S$	Radius of an idealized spherical cell containing a single gas bubble
$S_0$	Initial radius of an idealized spherical cell
$\alpha$	Volume fraction of bubbles
$N_d$	Bubble number density
$b, \beta$	Fitting parameters in the approximate pressure evolution (Equation 12)
$m_g$	Mas off the gas stored in a gas bubble and dissolved in a surrounding elementary cell
$C$	Gas concentration in the melt
$C_S$	Gas concentration st the saturation pressure $P_S$
$C_0$	Gas concentration st the nucleation pressure $P_0$
$a_r, b_r, a_c$	Coefficients in linear approximations for gas concentration and pressure
$\Pi$	Seismic potency
$M$	Seismic moment
$G$	Green's function
$\gamma_i$	Direction cosines
$r$	Source station distance
$V_p, V_S$	P and S seismic wave velocities

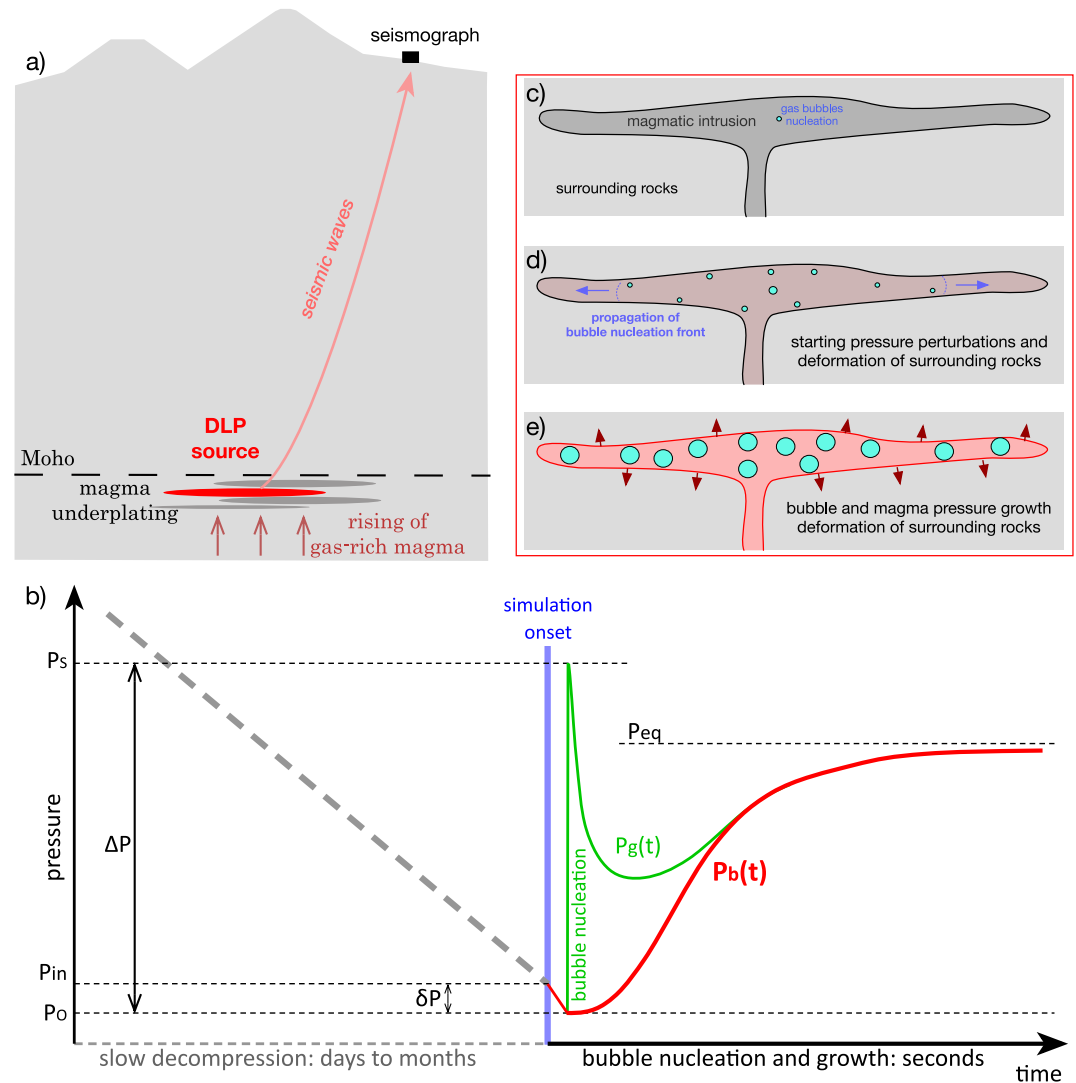


**Figure 1.** Schematic representation of the Deep Long Period source model. (a) General geometry with a source (a sill filled with a rapidly exsolving basaltic magma highlighted with the red color) located at the crust-mantle boundary and the station recording seismic waves located at the surface. (b) A schematic evolution of pressure in a model element containing magma. See Section 2.2.4 for details. (c)–(e) Main stages of the rapid bubble nucleation and growth of the magma within a sill.

sill (Figure 1d) causing its expansion (Figure 1e) and leading to elastic deformation of the surrounding rocks and generation of seismic waves recorded at the surface.

## 2.2. Mathematical Formulation for a Coupled Fluid-Solid System With Bubbles

In this study, we do not model microscopic processes of the gas bubble growth within the magma. Instead, we use the effective macroscopic behavior by approximating the results of model of O. Melnik et al. (2020) to describe how the magma pressure and effective macroscopic rheology vary in time. This model (briefly described in Appendix A) follows previous developments (e.g., B. Chouet et al., 2005, 2006; Lyakhovskiy et al., 1996; Nishimura, 2004; Prousevitch et al., 1993; Sparks, 1978) based on an approximation that represents the bubbly magma as a continuum of overlapping spherical cells of equal volumes, each containing an individual bubble and expanding because of its growth (e.g., Scriven, 1959) induced by diffusion of volatiles. O. Melnik et al. (2020) adopted this model for a case of simultaneous diffusion of two volatiles:  $H_2O$  and  $CO_2$ .

In all above mentioned models, the time varying pressure was approximated as spatially homogeneous within the whole considered magma volume. Based on this approximation, the pressure variations could be coupled to

deformation of the surrounding elastic media (rocks) and consequent generation of seismic waves when considering simplified geometries of the magma volume such crack or pipe and respective analytical expressions (Nishimura, 2004; B. Chouet et al., 2005, 2006; O. Melnik et al., 2020).

The main goal of our present work is to go beyond this approximation. Therefore, we develop a formalism in which the pressure is allowed to be spatially variable within the magmatic intrusion. Its space-time evolution is coupled with the space-time variations of mechanical stresses in the surrounding elastic media via the governing equations of the continuous mechanics that are solved numerically with a finite element approach. This solution is straightforward for elements containing rocks or bubble free magma (approximated as viscous fluid). For elements with bubbly magma, at each time step, we re-adjust the bubble volume fraction depending on the evolving volumetric stress (pressure) to satisfy the mass conservation as described in Section 2.2.4. This results in an effective rheology of the bubbly magma that is based on an approximate linearized functional dependence of gas concentration and density on pressure.

For simplicity, in the following, we describe application of this new modeling approach to a geometrically simple case of axially symmetric sill intrusion with initially homogeneous pressure distribution (that becomes spatially heterogeneous as a result of pressure and stress variations). At the same time, we note that the proposed numerical modeling can be directly applied to more complex geometries and pressure variations.

### 2.2.1. Governing Equations

We numerically solve the equations of continuum mechanics in a media consisting of a sill-shaped cavity filled with a viscous fluid (basaltic magma) embedded in an elastic medium (rocks). In the absence of body forces, the main dynamical equation is:

$$\rho \frac{\partial^2 u_i(x, t)}{\partial t^2} = \frac{\partial \sigma_{ij}(x, t)}{\partial x_j} \quad (2)$$

where  $\rho$ —material density;  $u_i(x, t)$ —displacement vector;  $\sigma_{ij}(x, t)$ —stress tensor. The total strain tensor  $\epsilon_{ij}^t(x, t)$  is calculated from the displacement field as:

$$\epsilon_{ij}^t(x, t) = \frac{1}{2} \left( \frac{\partial u_i(x, t)}{\partial x_j} + \frac{\partial u_j(x, t)}{\partial x_i} \right) \quad (3)$$

Different stress–strain constitutive relations (rheology) are adopted for model elements containing the surrounding rocks and the magma. Moreover, the behaviors of the initial bubble-free magma and of the one with growing bubbles are modeled differently. The surrounding rocks are modeled as linear elastic media. The bubble-free magma is modeled as a Maxwell visco-elastic body with very low elastic shear modulus. The effective time-variable rheology of the magma with bubble is approximated based on solution of O. Melnik et al. (2020). Details of these three different rheologies are described in the following subsections.

### 2.2.2. Solid Rock Rheology

The model elements containing the host rock are simulated as perfectly elastic isotropic Hookean solid ( $\epsilon_{ij}^t = \epsilon_{ij}^e$ , where upper index  $e$  corresponds to elastic deformations). The constitutive stress-strain relation for elastic deformations is:

$$\sigma_{ij} = \lambda_s \epsilon_{kk}^e \delta_{ij} + 2\mu_s \epsilon_{ij}^e \quad (4)$$

where  $\lambda_s$  and  $\mu_s$  are Lamé elastic moduli of the solid.

### 2.2.3. Rheology of Bubble-Free Magma

In the model elements containing the magma with the pressure that did not yet dropped below the critical value associated with the super-saturation of the gas dissolved in the melt, the magma remains bubble-free. In this state,

it is composed of basaltic melt that is approximated by Maxwell visco-elastic media with the total strain,  $\epsilon_{ij}^t$ , being a sum of the elastic,  $\epsilon_{ij}^e$  and irreversible (viscous deformation),  $\epsilon_{ij}^{irr}$ , strain components.

$$\epsilon_{ij}^t = \epsilon_{ij}^e + \epsilon_{ij}^{irr}, \quad (5)$$

The stress is separated in a deviatoric (zero-trace) component  $\tau_{ij}$  and volumetric pressure of the melt  $P_m$ :

$$\tau_{ij} = \sigma_{ij} + P_m \delta_{ij} \quad (6)$$

$$P_m = -\sigma_{kk}/3 \quad (7)$$

The deviatoric stress is related to the elastic strain via the magma shear modulus  $\mu_m$  and to the irreversible strain via a Newtonian stress—strain-rate relation with the melt viscosity  $\eta$

$$\tau_{ij} = 2\mu_m \epsilon_{ij}^e = \eta \frac{\partial \epsilon_{ij}^{irr}}{\partial t} \quad (8)$$

$\mu_m$  is set to be very small. As a result, the deviatoric stress in the magma is mainly controlled by the viscous deformation.

The pressure is related to the volumetric strain component  $\epsilon_v = -\epsilon_{kk}^t/3$  via the melt bulk modulus  $K_m$ :

$$P_m = K_m \epsilon_v \quad (9)$$

#### 2.2.4. Rheology of Bubbly Magma

In the model elements containing the magma where the nucleation condition is reached, bubbles nucleate and start to expand. In this case, the magma needs to be considered as mixture of melt and gas, although the bubble volume fraction remains small (less than 0.1%, O. Melnik et al. (2020)). As a consequence, Equation 9 must be modified to account for the added volume of gas. Also, we cannot consider the melt pressure  $P_m$  as main macroscopic variable. Instead we need to use the pressure of bubbly magma  $P_b$  that is not simply controlled by volumetric strain alone but also varies in time with bubble growth.

The dynamics of bubble growth under various conditions have been widely discussed in the literature (see reviews by Sparks (1978) and Gardner et al. (2023) and references therein). According to the bubble growth model (Lyakhovskiy et al., 1996; Prousevitch et al., 1993) the gas diffusion into the small bubble is very efficient at the initial stage of growth following the nucleation. The initial pressure difference or nucleation pressure is partly compensated by the surface tension term, which decreases as inverse of the bubble radius,  $1/R$ . The surface tension steeply decreases with the bubble growth and the pressure driving the bubble expansion practically remains constant. At this stage, the exponential increase of the bubble radius is controlled by the viscosity of the surrounding melt and the over-pressure,  $\Delta P$ , or the difference,  $\Delta P = P_s - P_0$ , between the saturation pressure,  $P_s$ , and the nucleation pressure in the surrounding melt,  $P_0$ . With the increase of the bubble radius, the efficiency of the diffusion decreases, and the rate of the bubble growth is controlled by the diffusive gas flux from the surrounding melt cell with a radius  $S$ . Finally, the bubble size and gas pressure approach their equilibrium values depending on the initial values of pressure, gas concentration, and cell size, as well as melt properties.

The initial cell size,  $S_0$ , or the melt volume surrounding every bubble may be calculated assuming certain number of bubbles nucleated from the unit melt volume, or bubble number density,  $N_d$ :

$$\frac{4}{3}\pi S_0^3 = \frac{1}{N_d} \quad (10)$$

The details of a single bubble growth model developed by (O. Melnik et al., 2020) consists of Raleigh-Lamb equation coupled with diffusion equations for two main dissolved volatile,  $H_2O$  and  $CO_2$ , and is briefly discussed in Appendix A. We apply this model to each magma-containing model element where the pressure dropped below the nucleation threshold  $P_0$ . The gas pressure inside the bubbles  $P_g$  just after nucleation is equal to



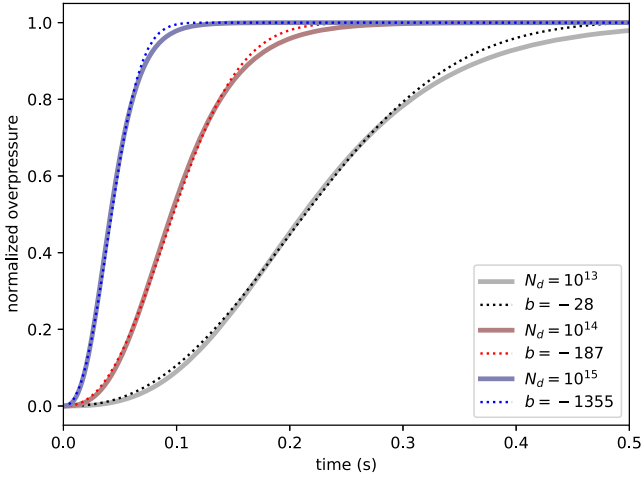


**Figure 2.** Normalized overpressure of the bubbly magma  $(P_b - P_0)/(P_{eq} - P_0)$  predicted by the model of O. Melnik et al. (2020) for different values of number density of bubbles.

the saturation pressure  $P_s$  (Lyakhovskiy et al., 1996). It is several tens of MPa higher than the initial pressure in the surrounding melt  $P_0$ . At final stage of the bubble growth both gas and melt  $P_m$  pressures approaches to the equilibrium pressure,  $P_{eq}$ . We can define the pressure in the bubbly magma  $P_b$  as:

$$P_b = P_g \alpha + P_m (1 - \alpha), \quad (11)$$

where  $\alpha$  is the volume fraction of bubbles,  $\alpha = \frac{R^3}{S_0^3}$ .

Figure 2 shows the overpressure,  $(P_b - P_0)/(P_{eq} - P_0)$ , evolution in the bubbly magma pocket simulated by the model from O. Melnik et al. (2020). Similar to this study, we consider compositions inferred for primary basaltic magma beneath Klychevskoy volcano in Kamchatka with 4 wt%  $H_2O$  and  $CO_2$  content estimated for a 828 MPa isobar (Mironov & Portnyagin, 2011; Portnyagin et al., 2007, 2019) and three different values of the bubble number densities,  $N_d = 10^{13}/m^3$  (gray line),  $N_d = 10^{14}/m^3$  (red line),  $N_d = 10^{15}/m^3$  (blue line). Here we use the initial over-pressure of  $\Delta P = P_s - P_0 = 40$  MPa (Shea, 2017). This pressure increase leads to a deformation of the surrounding rock mass and serves as a source pressure for the sill opening.

In our simulation, the gas bubbles are not triggered instantaneously in the whole volume. Therefore, the pressure increase is recalculated separately in every bubbly magma containing model element depending on the respective triggering time. For this goal, recomputing at every time step the solution of O. Melnik et al. (2020) is not practical. Therefore, we approximate these S-shaped pressure curves with a simple analytical function (shown with dotted lines in Figure 2):

$$(P_b - P_0)/(P_{eq} - P_0) = 1 - \exp(b t_n^\beta) \quad (12)$$

where  $t_n$  is time since the bubble nucleation and  $\beta = 2.4$  is the first fitting coefficient. The second fitting coefficient  $b$  significantly depends on the assumed bubble number density. The fitted values are:  $b = -28$  for  $N_d = 10^{13}/m^3$ ,  $b = -187$  for  $N_d = 10^{14}/m^3$ , and  $b = -1355$  for  $N_d = 10^{15}/m^3$ . Figure 2 shows the comparison between calculated and fitted pressure variations for different number density of bubbles.

To account for the effect of deformable elastic medium on the gas bubble growth, the equilibrium pressure  $P_{eq}$  in the every magma-containing model element is not set as a constant but is recomputed at every iteration depending on the deformation of the surrounding rock and volume change of the considered bubbly melt pocket. In this approximation, it varies with varying magma pressure  $P_b$ . This dependence  $P_{eq}(P_b)$  is calculated using the conservation the mass  $m_g$  of the gas stored in the bubble and dissolved in the surrounding elementary cell:

$$m_g = \frac{4}{3}\pi(S^3 - R^3)C\rho_m + \frac{4}{3}\pi R^3\rho_g = \frac{4}{3}\pi S_0^3 C\rho_m + \frac{4}{3}\pi R^3\rho_g = \frac{4}{3}\pi S_0^3 C_s\rho_m \quad (13)$$

where  $C_s$  is the gas concentration at the super-saturation needed for the bubble nucleation,  $\rho_m$  is the melt density that is assumed constant (we neglect its variations in comparison to the gas density changes). We use linear approximations, valid for small changes in pressure, for gas density,  $\rho_g$ :

$$\rho_g = a_r(P_b - P_0) + b_r \quad (14)$$

and dissolved gas concentration  $C$ :

$$C = a_c(P_b - P_0) + C_0 \quad (15)$$

with the following values taken from O. Melnik et al. (2020):  $a_c = 1.44 \times 10^{-5} \text{ MPa}^{-1}$ ,  $a_r = 0.586 \text{ kg/m}^3/\text{MPa}$ ,  $b_r = 902.5 \text{ kg/m}^3$ . The value of  $C_0$  defines the volatile concentration at pressure  $P_0$ .

With substituting these linear approximation into the gas mass balance Equation 13 and considering  $P_b = P_{eq}$  and  $P_b = P_s$  in its left and right sides, respectively, we obtain:

$$S_0^3 \rho_m (a_c (P_{eq} - P_0) + C_0) + R^3 (a_r (P_{eq} - P_0) + b_r) = S_0^3 \rho_m (a_c (P_s - P_0) + C_0) \quad (16)$$

and dividing by  $S_0^3$  leads to:

$$\rho_m (a_c (P_{eq} - P_0) + C_0) + \alpha (a_r (P_{eq} - P_0) + b_r) = \rho_m (a_c (P_s - P_0) + C_0) \quad (17)$$

By solving Equation 17 against  $P_{eq}$  we obtain the relation that adjusts equilibrium pressure in Equation 12

$$P_{eq} = \frac{\rho_m a_c P_s + \alpha (a_r P_0 - b_r)}{\alpha a_r + a_c \rho_m} \quad (18)$$

Equation 12 together with 18 govern the evolution of the source pressure in the bubbly magma. As soon as the nucleation condition is reached in particular cell instead of using Equation 9 to calculate the pressure from volumetric strain, we assume that the pressure is specified by Equation 12 and the volume fraction of bubbles is calculated as a difference between the total volume change and the elastic melt expansion:

$$\alpha = \varepsilon_v - P_b / K_m \quad (19)$$

Equation 18 together with 19 links the equilibrium pressure with the volumetric sill expansion. At the first time step of gas bubble growth, their volume fraction  $\alpha$  is equal to zero and from Equation 18 we obtain  $P_{eq} = P_s$ . Then, at every time step, we re-calculate the volumetric strain and estimate new values of  $\alpha$  and equilibrium pressure  $P_{eq}$  from Equations 18 and 19. Finally, the new value of  $P_b$  is estimated from 12 and is used in the new step of the time marching.

### 2.3. Generation of Seismic Waves

The deformation of the sill and surrounding media caused by the bubble growth generates a far reaching elastic field. If this deformation is sufficiently rapid, it will result in seismic waves transmitted into the surrounding elastic media and recorded by seismographs as volcanic earthquakes. To avoid excessive computations when calculating associated synthetic seismograms, we apply a standard separation of scales used in seismology. The details of the spatially heterogeneous source processes are computed within a small volume. The results of this computation are then coupled to a wave propagation in a simpler elastic media that can be described with associated Green's function. The seismic source associated with the magmatic sill and the deformation of the surrounding rocks can be seen as an ensemble of time variable equivalent mechanical forces arising from the inelastic deformation in the source region. Considering the small size of this source region ( $\sim 100 \text{ m}$ ) relative to distance along which the seismic waves propagate (tens of kilometers) and to the typical wavelength of the seismic waves within the crust (kilometers), these equivalent forces can be condensed into a point-source described by a nine-component tensor. This source description is not based on some particular geometry of the magmatic intrusion but is derived from the full results of the coupled fluid-elastic numerical simulation by integrating the irreversible strain over the source volume (e.g., Backus & Mulcahy, 1976; Ben-Menahem & Singh, 2012; Eshelby, 1957):

$$\Pi_{ij}(t) = \int_V \varepsilon_{ij}^{irr}(t) d^3x \quad (20)$$

This tensor  $\Pi_{ij}(t)$  is called potency or geometrical moment. Indexes  $i$  and  $j$  represent the cartesian coordinates (X, Y, Z). The integration volume in 20 is restricted to the sill because the irreversible strain vanishes outside it. The potency tensor is related to the more broadly known moment tensor  $M_{ij}(t)$  via the Hook stress-strain relation of the

host rock (e.g., Ben-Zion, 2003). This latter is modeled as an isotropic elastic media described with Lamé parameters  $\lambda_s$  and  $\mu_s$ , resulting in:

$$M_{ij}(t) = \lambda_s \Pi_{kk}(t) \delta_{ij} + 2\mu_s \Pi_{ij}(t) \quad (21)$$

Synthetic displacement seismograms are then computed as a convolution of the time-dependent seismic moment with the spatial derivatives of the Green's function (tensor)  $G$ :

$$u_n(t) = M_{p,q}(t) * G_{np,q} \quad (22)$$

where  $u_n(t)$  is the displacement in the cartesian direction  $n$ . For simplicity, we use the Green's function expression for a homogeneous and isotropic elastic media (Aki & Richards, 2002, Chapter 4, Equation 4.29) and only keep the far-field P- and S-wave terms. The near- and intermediate-field terms of the Green's function are ignored because the source-receiver distance is significantly larger than the wavelengths at dominant frequencies (above 1 Hz). The resulting displacement is then computed as:

$$u_n(t) = \frac{\gamma_n \gamma_p \gamma_q}{4\pi\rho V_p^3} \frac{1}{r} \dot{M}_{p,q} \left( t - \frac{r}{V_p} \right) - \left( \frac{\gamma_n \gamma_p - \delta_{np}}{4\pi\rho V_s^3} \right) \gamma_q \frac{1}{r} \dot{M}_{p,q} \left( t - \frac{r}{V_s} \right) \quad (23)$$

where  $r$  is the source-receiver distance,  $\rho$  is the media density, and  $V_p$  and  $V_s$  are P- and S- wave velocities, respectively.  $\gamma_i$  are direction cosines (in notations of Aki and Richards (2002)). The resulting displacement seismograms are composed of P and S arrivals with waveforms proportional to the first derivative of the time-dependent moment (potency) function and amplitudes controlled by combinations of source radiation patterns with geometrical spreading ( $\frac{1}{r}$ ). The velocity waveforms (typically recorded by seismic instruments) are then proportional to the second time derivative of the potency function.

### 3. Numerical Method and Model Settings

The 3D numerical modeling was performed using Explicit Finite Difference Lagrangian method, based on the FLAC (Fast Lagrangian Analyze of Continua) algorithm originally developed by Cundall (1988) for elastoplastic rheology and implemented in the ITASCA software. The FLAC algorithm was modified for viscoelastic media (Poliakov et al., 1993). A modified version of this code incorporating heat transport is known as PAROVOZ and is widely used by many researchers. Lyakhovsky et al. (2001) developed their own 3-D code for quasi-static visco-elastic damage rheology modeling, which was used in many geodynamic applications. Later on the code was modified for dynamic processes, by reducing force damping to realistic values corresponding to wave attenuation. The numerical time-step was defined according to the Courant–Friedrichs–Lewy stability condition for explicit time-marching simulations. Technical details of the numerical approach for dynamic modeling of seismic wave propagation were discussed by Lyakhovsky et al. (2016).

We considered several cases of the model geometry. Most of simulations were performed for the model volume  $200 \times 200 \times 100$  m with a 50 m radius and 3 m thick cylindrical sill located in the center (Figure 3a). In a few cases the model size have been doubled (both model dimensions and sill radius) keeping the same thickness. In the last series of the model runs two cylindrical sills with 40 m radius located in the same plain with three different distances, 40, 45, 50 m., between their edges (Figure 3b). The model was sampled with an adaptive grid with tetrahedral elements shown in Figure 4a. The smallest 0.5 m size elements are placed within the sill and their size gradually increases in vertical direction (Figure 4b).

Equation 2 is solved with fixed zero displacement boundaries with attached narrow layer of highly damping material that prohibits the reflection of waves traveling inside the host rock. The initial stress is equal to  $P_{in}$  with zero deviatoric components.

The elastic material surrounding the sill has the properties close to those of the mantle: the density  $\rho_s = 3000$  kg/m<sup>3</sup>, bulk modulus  $K_s = 80$  GPa, and rigidity (shear modulus)  $\mu_s = 50$  GPa. With these properties the seismic wave velocities in the host rock are:  $V_p = 7$  km/s,  $V_s = 4.1$  km/s. We considered physical properties of the melt inside the sill typical for basaltic compositions (e.g., Leshner & Spera, 2015). It is

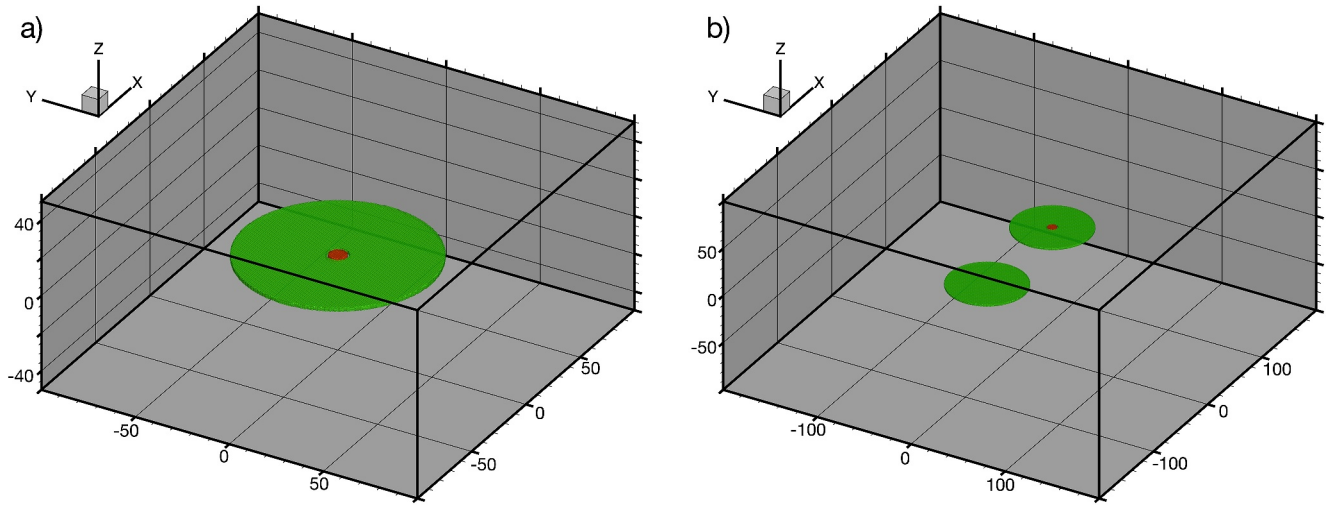


**Figure 3.** Geometries used in numerical simulations (dimensions are shown in meters). (a) A cylindrical sill of 50 m radius and 3 m thickness. Red color show the volume in which the bubble growth is triggered. (b) Two cylindrical sills of 40 m radius and 3 m thickness. The bubble growth is triggered in the center one of the sills (red color).

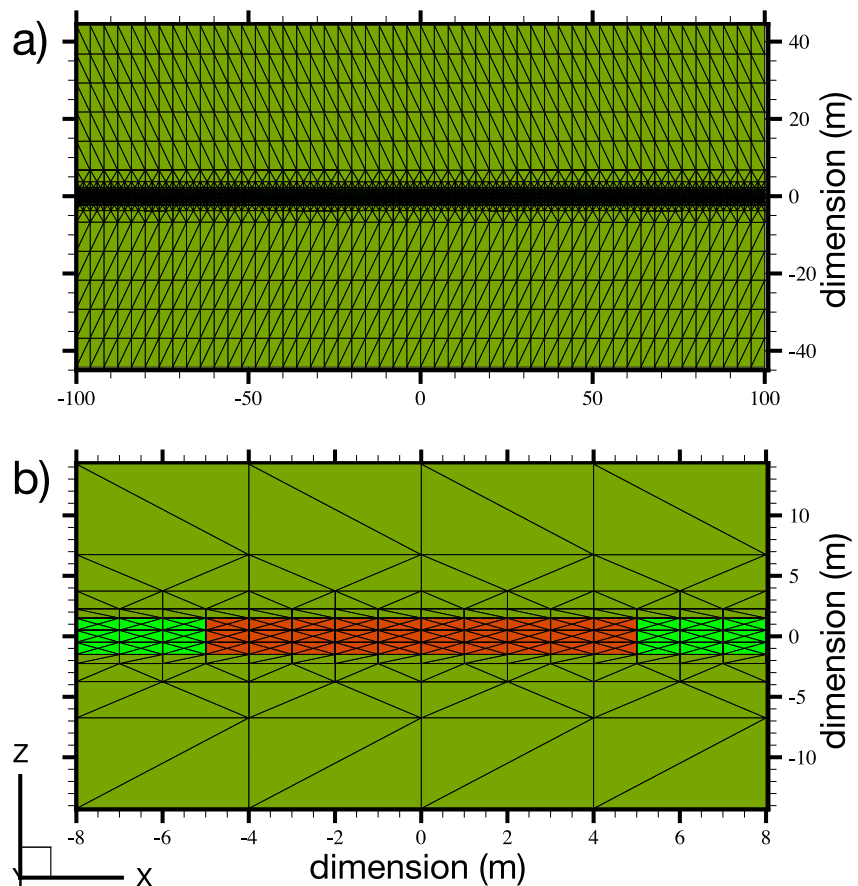


**Figure 4.** Adaptive grid with tetrahedral elements used for the numerical solution. (a) Cross-section the model shown in Figure 3a through the center of the sill in X direction. (b) Zoomed view of the grid surrounding the triggering region. Elements containing solid rocks and magma are shown with green and light green colors, respectively. The initial bubble growth is simultaneously triggered in the volume composed of elements indicated with the red color.

**Table 2**  
Main Parameters of the Tested Models

Run #	Model ID	Sill size (m)	Nd ( $1/m^3$ )	Nucleation threshold $\delta P$ (kPa)	Melt viscosity (Pa s)	Potency ( $m^3$ )
1	N1-A	50	$10^{13}$	10	100	22.33
2	N1-B	50	$10^{13}$	30	100	21.69
3	N1-C	50	$10^{13}$	50	100	20.24
4	N2-A	50	$10^{14}$	10	100	22.29
5	N2-B	50	$10^{14}$	30	100	22.13
6	N2-C	50	$10^{14}$	50	100	21.90
7	N3-A	50	$10^{15}$	10	100	22.12
8	N3-B	50	$10^{15}$	30	100	21.88
9	N3-C	50	$10^{15}$	50	100	21.65
10	N1-B V01	50	$10^{13}$	30	10	22.30
11	N1-B V10	50	$10^{13}$	30	1,000	22.36
12	N1-B L100	100	$10^{13}$	30	100	100.41
13	N4-1	2 × 40 Dist. 120	$3 \times 10^{13}$	20	100	28.69
14	N4-2	2 × 40 Dist. 125	$3 \times 10^{13}$	20	100	28.17
15	N4-3	2 × 40 Dist. 130	$3 \times 10^{13}$	20	100	14.39

characterized by a density of  $\rho_m = 2800 \text{ kg/cm}^3$ , a bulk modulus of 10 GPa, and a very low rigidity (5 orders of magnitude below the host rock rigidity). Melt viscosity ( $\eta$ ) varied between 10 and  $10^3$  Pa-s between different model runs. These values provide numerical stability of the Maxwellian visco-elastic solution with negligibly small elastic shear strain components in the melt. The shear stress in the melt is controlled by the product of the strain rate and melt viscosity, like in the Newtonian fluid. For the small volume fraction of bubbles the magma viscosity variations due to bubble content might be neglected. During the simulation the event potency is calculated by integrating the inelastic strain over the volume of the sill (Equation 20).

After estimating the potency tensor, we compute the propagation of seismic waves through the isotropic crust with average density of  $2,900 \text{ kg/m}^3$  and P- and S-wave velocities of 6,062 and 3,500 m/s, respectively. We consider a source-receiver distance of 30 km and a take-off angle at the source of  $15^\circ$ . This approximates the geometry with a curved seismic ray reaching a station located nearly above the source.

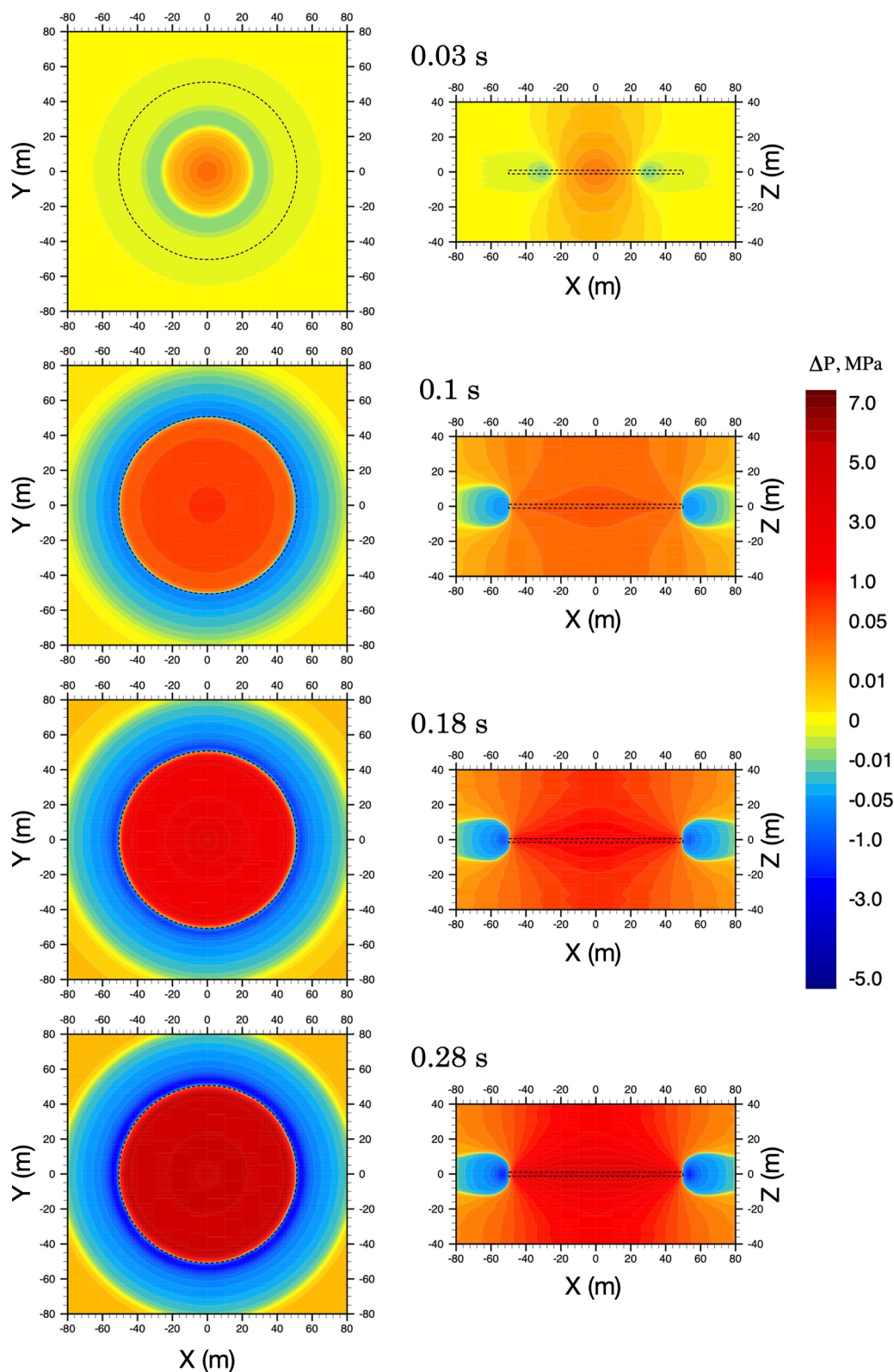
## 4. Results

During the study we considered 15 different models (see Table 2), 12 of them for a single sill (Figure 3a) and the last three for two discs (Figure 3b). All the simulations start with a spontaneous bubble nucleation in the 5-m circle area located in the center of the sill (red zone in Figure 3). In the case of a non-deformable surrounding material and adopted melt parameters, the maximal over-pressure may grow up to about 40 MPa in respect of the initial pressure  $P_0$ . However, its final value is significantly reduced because of the elastic deformation of the surrounding rock and the increase of the sill volume (see Equation 18).

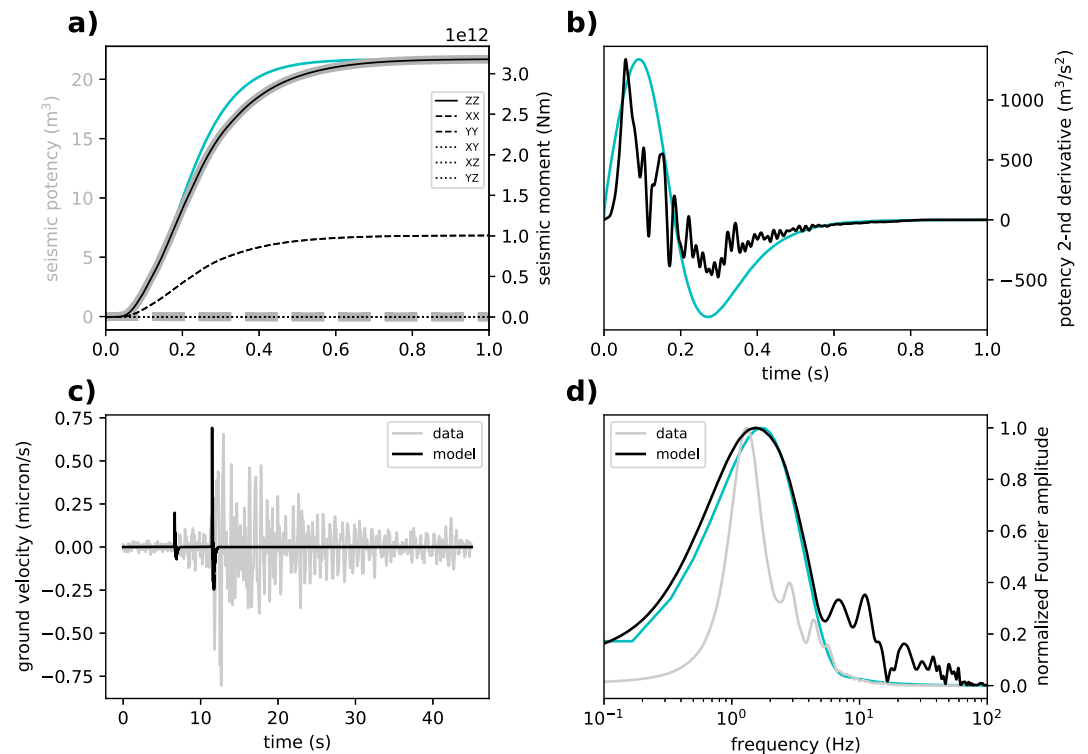
### 4.1. Single Sill Configuration

Figure 5 shows four horizontal and vertical cross sections for sequential snapshots of pressure (Equation 7) evolution for model N1-B (see Table 2 for parameters). Dashed lines on each cross section indicate the boundaries of the magmatic sill, where the bubble nucleation is expected.

The initial growth of the magma pressure in the nucleated zone (reddish colors) slightly increases the sill thickness in this area. This local “opening” is elastically transmitted toward to the surrounding region where it results in the local magma pressure decrease (bluish colors) leading to a new nucleation and bubble growth. The location of the narrow yellow ring between these zones corresponds to the radially propagating bubble nucleation front marked by transition from reduced to increased pressure. Therefore, the bubble nucleation front propagates as a pressure wave whose nature is different from a simple acoustic wave. The magma-filled sill acts as a wave guide in which



**Figure 5.** Snapshots of pressure (Equation 7) evolution in time in a model N1-B. Left and right frames show horizontal and vertical cross-sections at  $Z = 0$  and  $Y = 0$ , respectively. Time is indicated above the frames.



**Figure 6.** Seismic signature of model N1-B. (a) Components of potency (thick gray lines) and seismic moment (thin black lines) tensors as function of time. For comparison, cyan line shows normalized magma pressure computed for a case of instantaneous triggering of bubble growth (curve for 4 wt%  $H_2O$  from Figure 3 of O. Melnik et al. (2020)). (b) Second derivative of the ZZ potency function. For comparison, cyan line shows normalized second derivative of the O. Melnik et al. (2020) solution. (c) Comparison of synthetic and observed seismograms shown with black and gray lines, respectively. East-component seismogram of a Deep Long Period earthquake occurred on 26 June 2012 recorded at station LGN located on the slope of the Klyuchevskoy volcano (available at the repository: <https://zenodo.org/records/10409299> (<https://doi.org/10.5281/zenodo.10409299>)) (Lyakhovsky et al., 2024)) is shown as “data” (signal was high-passed at 0.5 Hz to remove the low-frequency ocean-generated microseismic noise). (d) Normalized Fourier amplitudes of signals shown in (c) smoothed in a 1 Hz wide moving window. For comparison, cyan line shows normalized Fourier amplitude of the O. Melnik et al. (2020) solution.

the elastic-acoustic coupling results in emergence of relatively slow “crack waves” propagating along the sill (e.g., B. Chouet, 1986, 1996; Maeda & Kumagai, 2017). The exact cylindrical symmetry is preserved during the sill expansion since the melt and surrounding rocks are homogeneous. The size of the area with the elevated pressure where the bubble are nucleated is about 20 m for the first snapshot and the nucleation front reaches the sill edge (50 m) during 0.1 s. This means that the nucleation front propagates at the rate of about 0.5 km/s.

Seismic source properties, synthetic seismograms, and their Fourier amplitude spectra for model N1-B are shown in Figure 6. As expected for vertically expanding horizontal sill, the potency tensor is dominated by the ZZ component. Its conversion into seismic moment with Equation 21 results in a diagonal tensor with ZZ component approximately three times larger than YY and XX (e.g., pure horizontal tensile crack). All three non-zero moment tensor components are proportional to the ZZ potency function whose time dependence defines the source time function. The body wave displacement and velocity is proportional to its first and second time derivatives, respectively. For comparison, the curves of magma pressure growth in a case of instantaneous triggering of bubble nucleation in a spherical batch of magma, that is, the solution of O. Melnik et al. (2020), are shown with cyan lines in Figures 6a and 6b. This comparison indicates that the effect of adding a pressure-dependant nucleation is relatively weak. The duration of the “source function” only slightly increases and it remains dominated by a low-frequency pulse corresponding to the kinetics of the bubble growth (Figure 6b). Similarly, the dominating frequency of the signal remains very low (1–2 Hz in Figure 6d) and is still controlled by the exsolution kinetics. At the same time, the non-instantaneous bubble nucleation results in small-scale heterogeneities of pressure within the magma. As a consequence, the guided “crack waves” (mentioned in the previous paragraph)

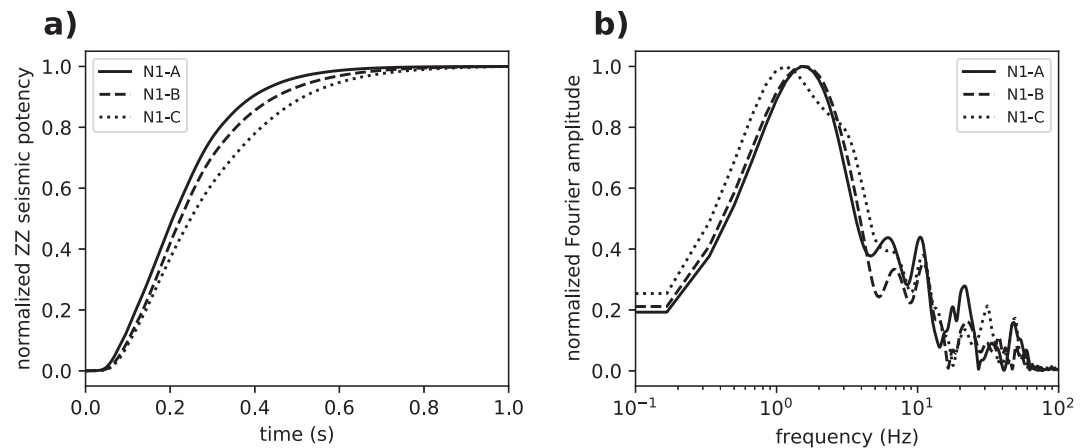


**Figure 7.** Influence of nucleation threshold  $\delta P$  on seismic source time functions. Three considered models differ by the value of this parameter: N1-A 10 kPa, N1-B 30 kPa, N1-C 50 kPa. (a) ZZ components of the seismic potency tensors as function of time. (b) Normalized Fourier amplitude of second derivatives of the ZZ potency function.

are excited and propagate within the sill and reflects on its edges. This leads to appearance of relatively weak high frequencies in the signal. Resulting synthetic seismograms (Figure 6c) contain both P and S waves with amplitudes close to the observations at station LGN whose location approximately corresponds to the modeling geometry described in the previous section. The frequency contents of observations and synthetics are also similar to each other (Figure 6d). However, the relatively long coda seen in the observed signal is not reproduced in the synthetic seismograms. One possible mechanism suggested for explaining long duration signals of volcanic LP earthquakes involves resonances of fluid filled cracks (e.g., B. A. Chouet, 1996; Maeda & Kumagai, 2017). Such resonance would arise from interference of “crack waves” reflected at the sill edges. However, our calculation show that, with the considered magma properties and the intrusion geometry, this effect is weak and is associated with frequencies much higher than the dominating observed peak ( $>8$  Hz in Figure 6d).

According to the fluid filled crack model, basaltic sills with large aspect ratios (narrower width and/or increased radius) would produce resonances at lower frequencies and with increased coda duration. Investigation of such large-aspect-ratio and regular-shape intrusions is out of scope of our study. We note that existence of such “homogeneous” features within very heterogeneous plumbing systems might be questionable where we could rather expect multiple intrusions with variable sizes and irregular shapes (e.g., O. E. Melnik et al., 2021). Therefore, we favor a hypotheses when the observed long coda mostly arises from the strong scattering of seismic waves within very heterogeneous volcanic media (e.g., Bracale et al., 2024; Kumagai et al., 2020; Wegler & Lühr, 2001). Explanation of such propagation effect would require using a more realistic Green's function.

For other cases with higher  $N_d$  values, the nucleation front propagates two (N2 series) and even more than three (N3 series) times faster. The bubble nucleation in the whole sill occurs relatively fast (0.1 s), while the overall duration of the sill expansion vary between 0.2 and 0.8 s for the series of nine model setting (lines 1–9 in Table 2). Therefore, the overall duration is mainly controlled by the kinetics of the bubble growth. The nucleation of new bubbles under appropriate conditions occurs extremely fast and the nucleation time scale is well below the time scale of the front propagation (for the discussed sill size) and future sill pressurization.

The bubbles nucleate when the over-saturation pressure is exceeded (e.g., Hirth et al., 1970). The level of the super-saturation depends on the temperature and a number of melt properties including surface tension, volume, and concentration of water molecules in the melt, as well as distance between them, diffusion coefficient of volatiles at the bubble-melt interface, probability that a nucleus at the top of the barrier will go on to form the new phase, rather than dissolve (Zeldovich factor), and others. With a huge uncertainty of these parameters and difficulties in their experimental constrain, we used three different values of the bubble number density ( $N_d = 10^{13}$ ,  $10^{14}$ , and  $10^{15}$  1/m<sup>3</sup>) (Sable et al., 2006) and nucleation thresholds ( $\delta P = 10$ , 30, and 50 kPa), assuming instantaneous nucleation when the target super-saturation is reached. Comparison of time-dependent potency for different simulations demonstrate that the pressurization rate weakly depends on the nucleation



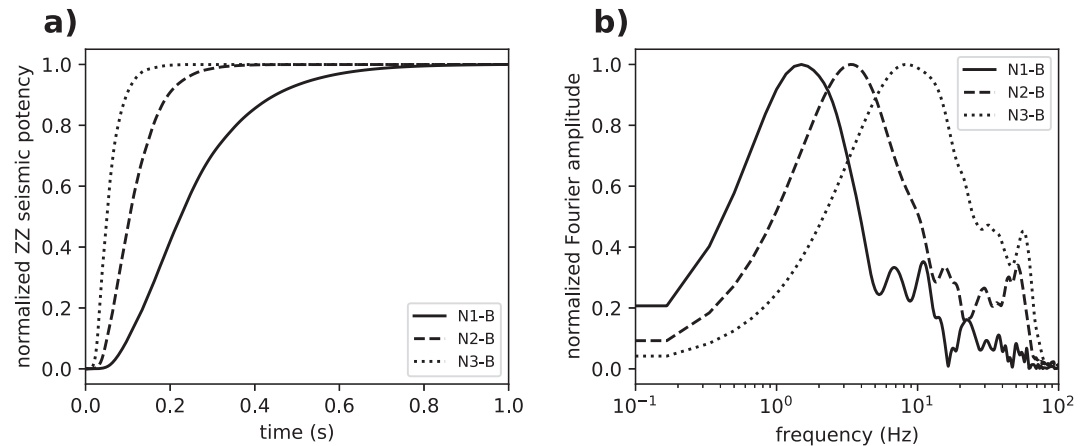


**Figure 8.** Influence of bubble number density  $N_d$  on seismic source time functions. Three considered models differ by the value of this parameter: N1-B  $10^{13}$ , N2-B  $10^{14}$ , N3-B  $10^{15}$ . (a) ZZ components of the seismic potency tensors as function of time. (b) Normalized Fourier amplitude of second derivatives of the ZZ potency function.

threshold,  $\delta P$  (Figure 7), and it is strongly affected by the bubble number density,  $N_d$  (Figure 8). The general pattern of the evolving pressure is very similar to the one shown in Figure 6, but differs only by the rate of pressurization. The sill expands significantly faster in the case with elevated  $N_d$  values.

Two additional simulations (10, 11 in Table 2) were performed to study a possible impact the melt viscosity, which was increased and decreases by an order of magnitude covering the realistic range of the basaltic melt properties (e.g., Leshner & Spera, 2015; Shaw, 1972). The difference in the pressurization rate (potency increase, not shown here) between these two cases and the model N1-B is negligibly small. The rate of the magma flow becomes important only at high viscosities (above  $10^5$  Pa s) typical for rhyolitic magmas (Hess & Dingwell, 1996) and controls the rate of sill pressurization.

Similarly to the classical seismological scaling relations we expect stronger event with larger potency (area times opening) proportional to the sill size. For the same pressure inside the sill with radius increased by a factor of two, we expect the sill opening to increase by a factor  $\sqrt{2}$ , since penny-shaped (cylindrical) crack opening is scaled as square root of the disc radius (Smith et al., 1967). Together with four times area increase (size in a power two), the potency should increase by a factor  $2^{2.5} \approx 5.66$ . However, opening of the sill leads to the reduction of the equilibrium pressure of the bubbly magma inside the sill. The results of the model N1-B-L100 show that the potency for the 100 m sill, instead of 50 m, is about  $100 \text{ m}^3$  meaning the increase by a factor 5 instead 5.66. The coupling between opening and pressure in the sill leads to a potency-area scaling with slightly deviates from the predictions of the linear elasticity ignoring the pressure-size dependency.

#### 4.2. Configuration With Two Sills

Expansion of the sill due to the bubble growth and pressurization leads to the deformation of the surrounding elastic media and formation of a relatively wide zone with a reduced pressure clearly seen in the last snapshots of Figure 5. This pressure reduction can initiate bubble nucleation in another sill or magma pocket located at a certain distance within the area of the negative pressure change (blue zone). Three last simulations demonstrate the sensitivity of the secondary nucleation to the distance between two discs (Figure 3b). In order to improve the numerical resolution without significantly increasing the computation time, we slightly decreased the disc radius to 40 m and placed the second disc at three different distances between their centers 130, 120, and 125 m (Table 2) or 50, 40, and 45 m between disc edges. Figure 9 shows the snapshots for the case N4-1. Slightly before 0.3 s the nucleation threshold (20 KPa) is achieved in the disc on the left and the nucleation starts on the right edge of this disc mostly affected by the pressurization of the first disc (snapshot 1 in Figure 9).

Seismic response of a two-sill system is illustrated in Figure 10 for model N4-2 (separation of 125 m). Nucleation of the first sill results in the initial rise of potency/moment values occurring between 0 and 0.3 s. This initial pulse is shorter than for model N1-B (Figure 6) and the dominant frequency higher mainly because of the smaller sill

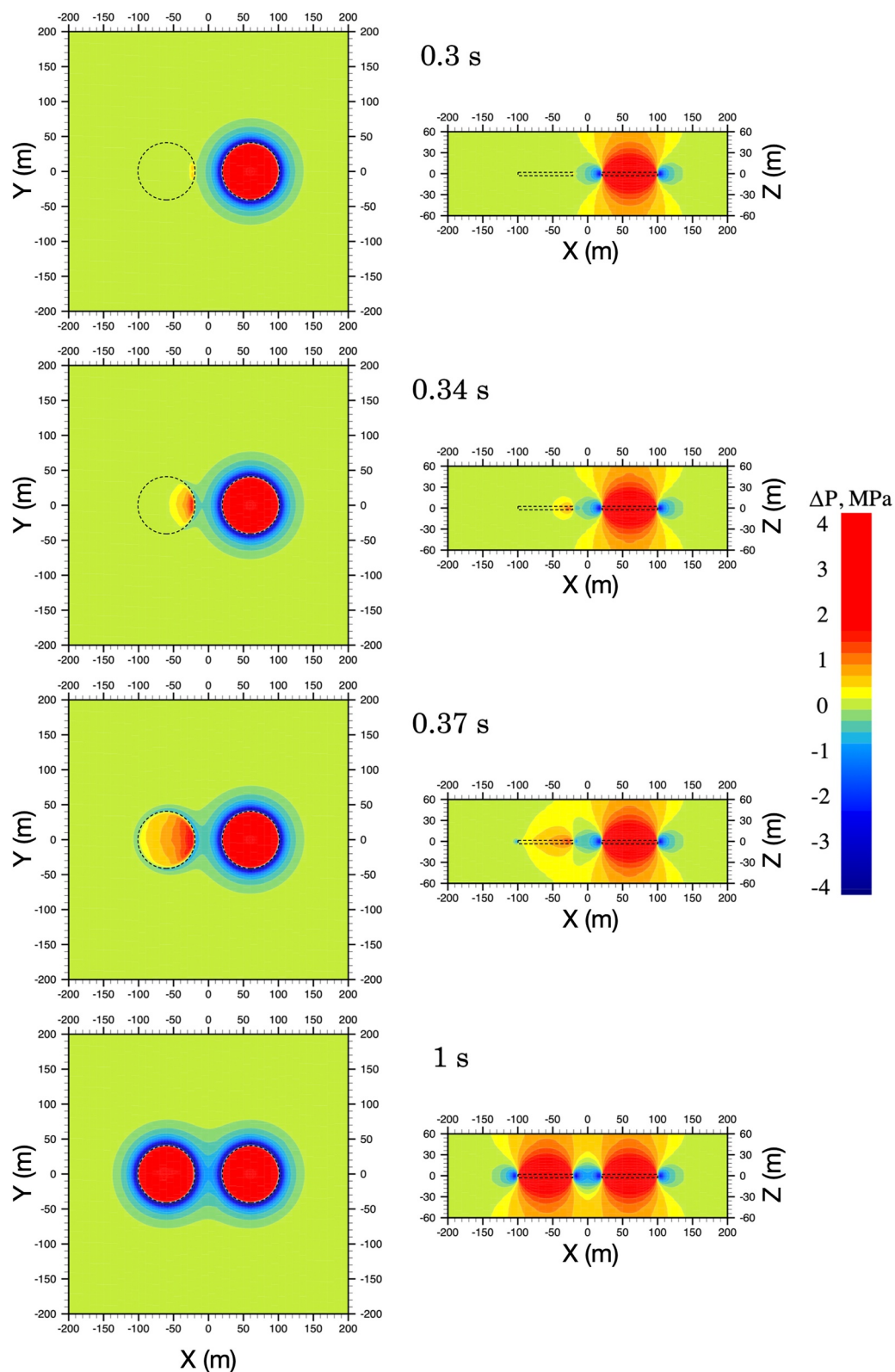


**Figure 9.** Snapshots of pressure (Equation 7) evolution in time in a model with two interacting sills (distance 120 m, model N4-1). Left and right frames show horizontal and vertical cross-sections at  $Z = 0$  and  $Y = 0$ , respectively. Times are indicated above the frames. Dashed lines indicate the boundaries of the magmatic sill.

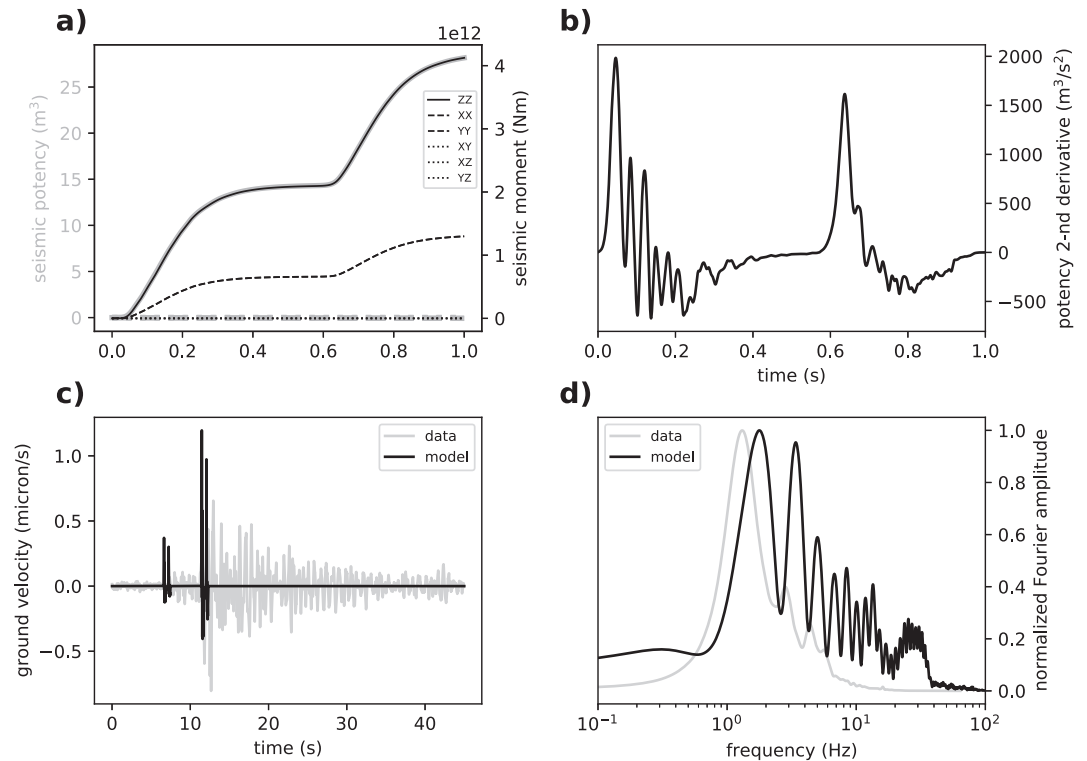


**Figure 10.** Similar to Figure 6 but model N4-2.

size. The bouncing of “crack waves” expressed in high frequencies seems to be more prominent in such smaller sill. The second sill nucleation starts at 0.6 s. The overall potency increases corresponding to two sills are nearly identical. At the same time, the second derivative of the potency function shows that the second impulse is relatively depleted in high frequencies. The reason for this is that the nucleation of the second sill starts not at the center but at the edge. As a result, the bouncing of “crack waves” is much less efficient.

The time delay for the second sill nucleation strongly depends on the distance between discs as shown in Figure 11. It increases from 0.3 to 0.6 s between separations of 120 and 125 m. For the 130 m distance between disc centers, the nucleation threshold is never achieved. After the nucleation occurred, the nucleation front propagates toward the opposite edge of the disc with the rate controlled by the bubble growth parameters as

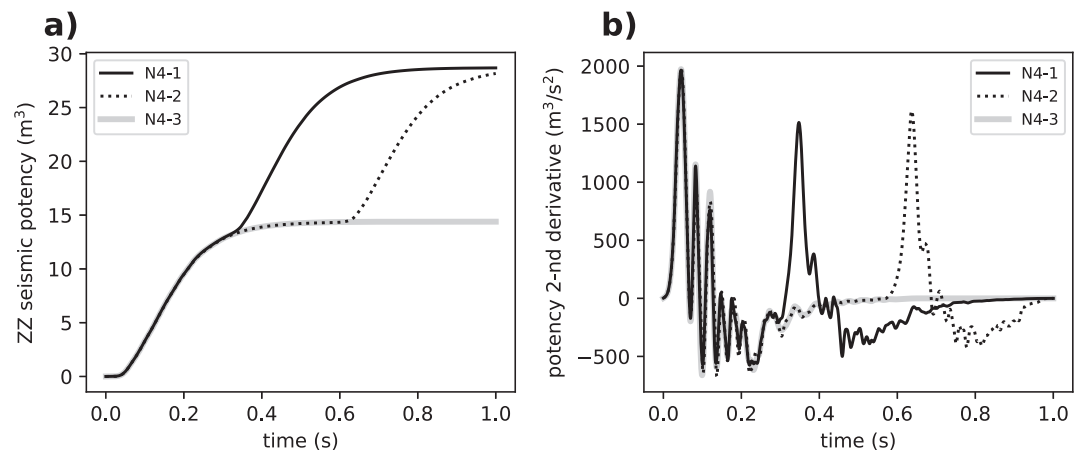


**Figure 11.** Comparison of seismic source time functions for models with two sills. (a) ZZ components of the seismic potency tensors as function of time. (b) Second derivatives of the ZZ potency function.

discussed above. With pressure growth increase in both discs, the size of zone with a reduced pressure (blue colors) increases and may provoke nucleation in additional magma pockets, not necessarily aligned in the same plane. Vertical cross sections clearly demonstrate significant increase of the negative pressure zone in the  $Z$ -direction. Comparison between three cases of the N4 series shows that there exist certain critical distance for the secondary nucleation and the delay time strongly depends on this distance.

## 5. Discussion and Conclusions

We developed an accurate model of generation of seismic waves by the pressure variations caused by bubble growth in the basaltic magma. This model is based on a numerical solution of a fluid-elastic coupled equations and includes a bubble nucleation front propagating from initial trigger point in a sill-shaped magma intrusion.

The results of our simulations confirm the hypotheses of O. Melnik et al. (2020) that the rapid growth of gas bubbles within magmatic intrusions can generate seismic waves with amplitudes and spectral content similar to those observed from DLP earthquakes. In particular, we show that with modeling realistic shapes of the intrusions such as sills, a mostly volumetric expansion results in generation of stronger S waves than P waves. Our simulations show that realistic amplitudes can be predicted with modeling sills of  $\sim 50$  m of radius and  $\sim 1$  m of thickness. The object of such dimensions can correspond either to an individual small sill or to a pocket of oversaturated magma within larger intrusions.

Additionally, our modeling shows that bubble nucleation front propagation is controlled by the coupled elasto-acoustic waves. For the selected sill dimensions, this propagation is rapid comparing to the kinetics of the bubble growth and the bubble growth dominates the source time function and the spectral content of the emitted signals. This kinetics is controlled by the bubble number density  $N_d$  and the gas content in the magma (O. Melnik et al., 2020). Explaining the observed DLP signal properties with the effect of bouncing of “crack waves” eventually leading to resonances of fluid filled cracks (e.g., B. Chouet, 1986; B. A. Chouet, 1996; Maeda & Kumagai, 2017) would require to consider very thin and extended regular-shaped sills whose existence within a heterogeneous plumbing system might be questionable.

The large uncertainty in the model parameters can lead to large differences in the duration, amplitude, and frequency content of synthetic earthquake signals. A full statistical study of the influence of governing parameters on earthquake characteristics is outside the scope of the paper because of large computational costs of a single scenario. All qualitative dependencies on such parameters as the volatiles content, the bubble number density, the melt viscosity etc., investigated in (O. Melnik et al., 2020) remain valid. Additional uncertainties rise from possible different sizes and shapes of the magma pockets and more prolonged duration of the signal due to unsynchronized bubble nucleation in different parts of the intrusion.

The results of our modeling presented in Section 4.2 highlight a possibility of “interaction” between closely located intrusions when the elastic deformation caused by the gas exsolution leading to expansion of the first sill can trigger the bubble nucleation in the next closely located magma pocket. We presented simulations for two “interacting” sills. This results can be extrapolated to a case of many closely located magma pockets acting in a cascade. Such behavior can explain the observation of DLP earthquakes often occurring as swarms of many events closely located in time (e.g., Shapiro, Droznin, et al., 2017; Song et al., 2023; White et al., 1996) eventually leading to emergence of deep volcanic tremors (e.g., Aki & Koyanagi, 1981; Journeau et al., 2022; Soubestre et al., 2019).

The emergence of tremors would become favorable in a configuration where many “interacting” pockets of oversaturated magma are closely located. The results shown in Figure 11 demonstrate that with the selected model parameters and in approximation of in-plane circular sills, the interaction becomes possible when inter-sill distance approaches the sill radius. The “interaction” distance would then increase with decreasing the nucleation threshold. The time delay between two “interacting events” would increase with increasing the inter-sill distance and also with decreasing the bubble number density.

More generally, some scaling relations based on the stress distribution around a pressurized inclusion could be considered. The linear elasticity predicts that the pressure distribution around the inclusion is proportional to the overpressure and decreases as a polynomial function of the ratio  $\frac{R}{d}$  ( $R$ —disc radius,  $d$ —distance from the inclusion center). Near the edge of the inclusion the forth order term,  $(\frac{R}{d})^4$ , is dominant and defines fast pressure decay away

from the inclusion. The width of the zone with the negative pressure is expected to be of the order of the inclusion size. For a given distance,  $d$ , from the inclusion, the nucleation occurs when the pressure in the inclusion drops below certain critical value, which linearly increases with the nucleation threshold and decreases as  $(\frac{R}{d})^4$ , which is the dominant term for the near-field solution.

The processes of the diffusion-driven bubble growth coupled with the elasticity of the surrounding rock matrix is highly nonlinear and our modeling approach is based on several simplifications and approximations as described in the above text. In particular, we approximate the bubble nucleation as instantaneous which is valid for small volumes of basaltic magma (O. Melnik et al., 2020). The processes of the diffusive bubble growth is approximated with a simple analytical function that fits a numerical solution (Figure 2, Equation 12). The effect of deformable elastic medium on the gas bubble growth is approximated with adjusting the equilibrium pressure  $P_{eq}$  in Equation 12 at every iteration based on a simplified linearized functional dependence of gas concentration and density on pressure.

We note that the modeling framework proposed in our paper makes a step forward with respect to previous studies of the bubble growth in magma (e.g., B. Chouet et al., 2005, 2006; Lyakhovskiy et al., 1996; O. Melnik et al., 2020; Nishimura, 2004; Prousevitch et al., 1993) by going beyond the approximation of spatially homogeneous pressure in the whole magma volume. In our approach, the space-time evolution of magma pressure is coupled with the space-time variations of mechanical stresses in the surrounding elastic media via a full numerical solution of the governing equations of the continuous mechanics. Therefore, the presented modeling frameworks can be applied to magma pockets of arbitrary shapes. One possible direction of its application to better understand the origin of deep volcanic tremors would be to investigate the cascading of gas exsolution in a system containing many sills and dykes with variable sizes (e.g., Bindeman et al., 2023; O. E. Melnik et al., 2021). A more challenging and important task would be to move from a “static” systems of interacting magma pockets and to model their time evolution and, in particular, their refilling with fresh magma and volatiles which is necessary for functioning of sustained generation of deep volcanic seismicity.

## Appendix A: Single Bubble Growth Model

The model of O. Melnik et al. (2020) is based on a representation of bubbly magma as a continuum of overlapping spherical cells (Prousevitch et al., 1993), each containing an individual bubble, that is widely used for modeling the bubble growth in the magma (e.g., Sparks, 1978; Lyakhovskiy et al., 1996; Nishimura, 2004; B. Chouet et al., 2005, 2006). It assumes that the total volume of a magma batch is divided to  $N$  individual cells of the same volume, which expand with a growing bubble and supply volatiles into it. The flow around each bubble is assumed spherically symmetric.

The process of an individual bubble growth from a supersaturated magma is described by a set of Rayleigh-Lamb equations together with diffusion equations for two main dissolved volatiles,  $H_2O$  and  $CO_2$ :

$$\frac{\partial}{\partial r}(r^2 \nu_r) = 0; \nu_r|_{r=R} = \frac{dR}{dt}; \quad (A1)$$

$$P_g - P_m = \frac{2\sigma}{R} + 4\mu \frac{dR}{dt} \left( \frac{1}{R} - \frac{R^2}{S^3} \right); \quad (A2)$$

$$P_m = P_m^0 + \frac{4}{3}G \left( \frac{S^3 - S_0^3}{S_0^3} \right); \quad (A3)$$

$$\frac{\partial c_s}{\partial t} + \nu_r \frac{\partial c_s}{\partial r} = \frac{1}{r^2} \frac{\partial}{\partial r} \left( D_s r^2 \frac{\partial c_s}{\partial r} \right); \quad (A4)$$

$$\frac{4\pi}{3} \frac{d}{dt} (R^3 \rho_g x_{CO_2}^b) = 4\pi R^2 J_c; \quad (A5)$$

$$\frac{4\pi}{3} \frac{d}{dt} (R^3 \rho_g (1 - x_{CO_2}^b)) = 4\pi R^2 J_w; \quad (A6)$$

$$J_c = -D_c \rho_m \left( \frac{\partial c_c}{\partial r} \right)_{r=R}; J_w = -D_w \rho_m \left( \frac{\partial c_w}{\partial r} \right)_{r=R}. \quad (A7)$$

$$\rho_g = \left( \frac{x_{CO_2}^b}{\rho_{CO_2}(P_g, T)} + \frac{1 - x_{CO_2}^b}{\rho_{H_2O}(P_g, T)} \right)^{-1}; \quad (A8)$$

$$\rho_{CO_2} = (0.371 + 0.13 \times 10^{-3} T) P_g + 1194.65 - 0.4665 T; \quad (A9)$$

$$\rho_{H_2O} = (0.22 + 0.13 \times 10^{-3} T) P_g + 892.2 - 0.357 T; \quad (A10)$$

$$D_w = c_w \exp \left( -8.56 - \frac{19110}{T} \right); \quad (A11)$$

$$D_c = \exp \left( -13.99 - \frac{(17367 + 1.945 P_g)}{T} + \frac{c_w (855.2 + 0.271 P_g)}{T} \right) \quad (A12)$$

Here  $t$  is time,  $r$  is the radial coordinate,  $R$  is the radius of the bubble,  $v_r$  is the radial velocity, index  $s = w, c$  corresponds to water and carbon dioxide, respectively,  $c_c$  and  $c_w$  are the mass concentrations of CO<sub>2</sub> and H<sub>2</sub>O in the melt,  $D_c$  and  $D_w$  are the volatile diffusion coefficients,  $J_c$  and  $J_w$  are diffusive fluxes,  $P_g$  is the pressure of the gas inside the bubble,  $P_m$  is the melt pressure,  $S$  is the diameter of the melt cell, from which the bubble is growing, index “0” corresponds to initial values,  $\sigma$  is the surface tension,  $\mu$  is the magma viscosity,  $G$  is the shear modulus of the host rock,  $\rho_g$  is the density of the gas in the bubble that depends on the pressure, temperature  $T$  and bubble volatile composition  $x_{CO_2}^b$ .

The densities of pure CO<sub>2</sub> ( $\rho_{CO_2}$ ) and H<sub>2</sub>O ( $\rho_{H_2O}$ ) are approximated at a limited  $P - T$  range using tables produced by NIST Chemistry WebBook (<https://webbook.nist.gov/chemistry/>).

Diffusion Equation A4 are subjected to two boundary conditions: concentration gradients are equal to zero at the outer surfaces of the cell mimicking symmetry of the system. At  $r = R(t)$  volatiles in magma are in chemical equilibrium with the bubble. Thus,  $c_s = c_s^{eq}(P_g, T, x_{CO_2}^b)$ .

## Data Availability Statement

The algorithm and its implementation for the 3-D modeling of quasi-static visco-elastic damage rheology are described in Lyakhovskiy et al. (2001). The relevant details regarding the execution of model simulations are described in this manuscript. The fortran code used to carry out the calculations as well as the relevant input and output files together with the python script and the real data seismogram shown in Figure 6 used for their visualization are available at (Lyakhovskiy et al., 2024).

## Acknowledgments

This study was supported by the European Research Council under the European Union Horizon 2020 research and innovation program (Grant Agreement 787399-SEISMAZE). The work of OM was supported by French Governmental program PAUSE (Programme d'Aide à l'Accueil des Scientifiques en Urgence).

## References

- Aki, K., & Koyanagi, R. (1981). Deep volcanic tremor and magma ascent mechanism under Kilauea, Hawaii. *Journal of Geophysical Research*, 86(B8), 7095–7109. <https://doi.org/10.1029/JB086iB08p07095>
- Aki, K., & Richards, P. G. (2002). *Quantitative seismology* (2nd ed.). University Science Books. Hardcover. Retrieved from <http://www.worldcat.org/isbn/0935702962>
- Aso, N., & Ide, S. (2014). Focal mechanisms of deep low-frequency earthquakes in Eastern Shimane in Western Japan. *Journal of Geophysical Research: Solid Earth*, 119(1), 364–377. <https://doi.org/10.1002/2013JB010681>
- Aso, N., Ohta, K., & Ide, S. (2013). Tectonic, volcanic, and semi-volcanic deep low-frequency earthquakes in western Japan. *Tectonophysics*, 600, 27–40. (Great Earthquakes along Subduction Zones). <https://doi.org/10.1016/j.tecto.2012.12.015>
- Aso, N., & Tsai, V. C. (2014). Cooling magma model for deep volcanic long-period earthquakes. *Journal of Geophysical Research: Solid Earth*, 119(11), 8442–8456. <https://doi.org/10.1002/2014JB011180>
- Backus, G., & Mulcahy, M. (1976). Moment tensors and other phenomenological descriptions of seismic sources—I. Continuous displacements. *Geophysical Journal International*, 46(2), 341–361. <https://doi.org/10.1111/j.1365-246X.1976.tb04162.x>
- Ben-Menahem, A., & Singh, S. J. (2012). *Seismic waves and sources*. Springer Science & Business Media.
- Ben-Zion, Y. (2003). Appendix 2 - Key formulas in earthquake seismology. In W. H. Lee, H. Kanamori, P. C. Jennings, & C. Kisslinger (Eds.), *International handbook of earthquake and engineering seismology, Part B* (Vol. 81, pp. 1857–1875). Academic Press. [https://doi.org/10.1016/S0074-6142\(03\)80304-2](https://doi.org/10.1016/S0074-6142(03)80304-2)
- Bindeman, I. N., Melnik, O. E., Guillong, M., Utkin, I. S., Wotzlaw, J. F., Schmitt, A. K., & Stern, R. A. (2023). Age of the magma chamber and its physicochemical state under Elbrus greater Caucasus, Russia using zircon petrochronology and modeling insights. *Scientific Reports*, 13(1), 9733. <https://doi.org/10.1038/s41598-023-36793-y>

- Bracale, M., Campillo, M., Shapiro, N. M., Brossier, R., & Melnik, O. (2024). The influence of multiple scattered waves on the spectral stability of volcanic tremors. In *Paper presented at the annual meeting of seismological society of America, Anchorage, Alaska*.
- Burgisser, A., Alletti, M., & Scaillet, B. (2015a). D-compress. Retrieved from <https://thehub.org/resources/3791>
- Burgisser, A., Alletti, M., & Scaillet, B. (2015b). Simulating the behavior of volatiles belonging to the c–o–h–s system in silicate melts under magmatic conditions with the software d-compress. *Computers & Geosciences*, 79, 1–14. <https://doi.org/10.1016/j.cageo.2015.03.002>
- Cassidy, M., Manga, M., Cashman, K., & Bachmann, O. (2018). Controls on explosive-effusive volcanic eruption styles. *Nature Communications*, 9(1), 2839. <https://doi.org/10.1038/s41467-018-05293-3>
- Chouet, B. (1986). Dynamics of a fluid-driven crack in three dimensions by the finite difference method. *Journal of Geophysical Research*, 91(B14), 13967–13992. <https://doi.org/10.1029/JB091iB14p13967>
- Chouet, B., Dawson, P., & Arciniega-Ceballos, A. (2005). Source mechanism of Vulcanian degassing at Popocatepetl volcano, Mexico, determined from waveform inversions of very long period signals. *Journal of Geophysical Research*, 110(B7). <https://doi.org/10.1029/2004JB003524>
- Chouet, B., Dawson, P., & Nakano, M. (2006). Dynamics of diffusive bubble growth and pressure recovery in a bubbly rhyolitic melt embedded in an elastic solid. *Journal of Geophysical Research*, 111(B7). <https://doi.org/10.1029/2005JB004174>
- Chouet, B. A. (1996). Long-period volcano seismicity: Its source and use in eruption forecasting. *Nature*, 380(6572), 309–316. <https://doi.org/10.1038/380309a0>
- Cundall, P. A. (1988). Numerical experiments on localization in frictional materials. In *Proc. of the workshop on limit analysis and bifurcation theory*.
- Eshelby, J. D. (1957). The determination of the elastic field of an ellipsoidal inclusion, and related problems. *Proceedings of the Royal Society of London. Series A. Mathematical and Physical Sciences*, 241(1226), 376–396. <https://doi.org/10.1098/rspa.1957.0133>
- Fedotov, S. A., Zharinov, N. A., & Gontovaya, L. I. (2010). The magmatic system of the Klyuchevskaya group of volcanoes inferred from data on its eruptions, earthquakes, deformation, and deep structure. *Journal of Volcanology and Geothermal Research*, 4(1), 1–33. <https://doi.org/10.1134/S074204631001001X>
- Galina, N. A., & Shapiro, N. M. (2024). Source mechanisms of deep long period earthquakes beneath the Klyuchevskoy volcanic group (Kamchatka, Russia) inferred from s-to-p amplitude ratios. *Journal of Volcanology and Geothermal Research*, 448, 108049. <https://doi.org/10.1016/j.jvolgeores.2024.108049>
- Galina, N. A., Shapiro, N. M., Droznina, D. V., Droznina, S. Y., Senyukov, S. L., & Chebrov, D. V. (2020). Recurrence of deep long-period earthquakes beneath the Klyuchevskoi volcano group, Kamchatka. *Izvestiya - Physics of the Solid Earth*, 56(6), 749–761. <https://doi.org/10.1134/S1069351320060026>
- Gardner, J. E., Wadsworth, F. B., Carley, T. L., Llewellyn, E. W., Kusumaatmaja, H., & Sahagian, D. (2023). Bubble formation in magma. *Annual Review of Earth and Planetary Sciences*, 51(1), 131–154. <https://doi.org/10.1146/annurev-earth-031621-080308>
- Greenfield, T., Winder, T., Rawlinson, N., MacLennan, J., White, R. S., Ágústsdóttir, T., et al. (2022). Deep long period seismicity preceding and during the 2021 Fagradalsfjall eruption, Iceland. *Bulletin of Volcanology*, 84(12), 101. <https://doi.org/10.1007/s00445-022-01603-2>
- Hensch, M., Dahm, T., Ritter, J., Heimann, S., Schmidt, B., Stange, S., & Lehmann, K. (2019). Deep low-frequency earthquakes reveal ongoing magmatic recharge beneath Laacher See Volcano (Eifel, Germany). *Geophysical Journal International*, 216(3), 2025–2036. <https://doi.org/10.1093/gji/ggy532>
- Hess, K., & Dingwell, D. B. (1996). Viscosities of hydrous leucogranitic melts: A non-arrhenian model. *American Mineralogist: Journal of Earth and Planetary Materials*, 81(9–10), 1297–1300.
- Hirth, J., Pound, G., & St. Pierre, G. (1970). Bubble nucleation. *Metallurgical Transactions A*, 1(4), 939–945. <https://doi.org/10.1007/BF02811776>
- Iacovino, K., Matthews, S., Wieser, P. E., Moore, G. M., & Bégué, F. (2021). Vesical Part I: An open-source thermodynamic model engine for mixed volatile (H<sub>2</sub>O–CO<sub>2</sub>) solubility in silicate melts. *Earth and Space Science*, 8(11), e2020EA001584. <https://doi.org/10.1029/2020EA001584>
- Ikegaya, T., & Yamamoto, M. (2021). Spatio-temporal characteristics and focal mechanisms of deep low-frequency earthquakes beneath the Zao volcano, northeastern Japan. *Journal of Volcanology and Geothermal Research*, 417, 107321. <https://doi.org/10.1016/j.jvolgeores.2021.107321>
- Jaupart, C., & Vergnolle, S. (1988). Laboratory models of Hawaiian and strombolian eruptions. *Nature*, 331(6151), 58–60. <https://doi.org/10.1038/331058a0>
- Journeau, C., Shapiro, L. N. M., Seydoux, L., Soubestre, J., Koulakov, I. Y., Jakovlev, A. V., et al. (2022). Seismic tremor reveals active trans-crustal magmatic system beneath Kamchatka volcanoes. *Science Advances*, 8(5), eabj1571. <https://doi.org/10.1126/sciadv.abj1571>
- Koulakov, I., Shapiro, N. M., Sens-Schönfelder, C., Luehr, B. G., Gordeev, E. I., Jakovlev, A., et al. (2020). Mantle and crustal sources of magmatic activity of Klyuchevskoy and surrounding volcanoes in Kamchatka inferred from earthquake tomography. *Journal of Geophysical Research: Solid Earth*, 125(10), e2020JB020097. <https://doi.org/10.1029/2020JB020097>
- Kumagai, H., Torres, R., & Maeda, Y. (2020). Scattering and attenuation characteristics at volcanoes inferred from envelope widths of natural and active seismic sources. *Journal of Geophysical Research: Solid Earth*, 125(11), e2020JB020249. <https://doi.org/10.1029/2020JB020249>
- Kurihara, R., & Obara, K. (2021). Spatiotemporal characteristics of relocated deep low-frequency earthquakes beneath 52 volcanic regions in Japan over an analysis period of 14 years and 9 months. *Journal of Geophysical Research: Solid Earth*, 126(10), e2021JB022173. <https://doi.org/10.1029/2021JB022173>
- Kurihara, R., Obara, K., Takeo, A., & Tanaka, Y. (2019). Deep low-frequency earthquakes associated with the eruptions of Shinmoe-Dake in Kirishima volcanoes. *Journal of Geophysical Research: Solid Earth*, 124(12), 13079–13095. <https://doi.org/10.1029/2019JB018032>
- Lensky, N. G., Niebo, R. W., Holloway, J. R., Lyakhovskiy, V., & Navon, O. (2006). Bubble nucleation as a trigger for xenolith entrapment in mantle melts. *Earth and Planetary Science Letters*, 245(1), 278–288. <https://doi.org/10.1016/j.epsl.2005.11.064>
- Leshner, C. E., & Spera, F. J. (2015). Chapter 5 - Thermodynamic and transport properties of silicate melts and magma. In H. Sigurdsson (Ed.), *The encyclopedia of volcanoes* (2nd ed., pp. 113–141). Academic Press. <https://doi.org/10.1016/B978-0-12-385938-9.00005-5>
- Levin, V., Droznina, S. Y., Gavrilenko, M., Carr, M. J., & Senyukov, S. L. (2014). Seismically active subcrustal magma source of the Klyuchevskoy volcano in Kamchatka, Russia. *Geologica*, 42(11), 983–986. <https://doi.org/10.1130/G35972.1>
- Lu, L., & Bostock, M. G. (2022). Deep long-period earthquakes near mount meager, British Columbia. *Canadian Journal of Earth Sciences*, 59(7), 407–417. <https://doi.org/10.1139/cjes-2021-0103>
- Lyakhovskiy, V., Ben-Zion, Y., Ilchev, A., & Mendecki, A. (2016). Dynamic rupture in a damage-breakage rheology model. *Geophysical Journal International*, 206(2), 1126–1143. <https://doi.org/10.1093/gji/ggw183>
- Lyakhovskiy, V., Hurwitz, S., & Navon, O. (1996). Bubble growth in Rhyolitic melts: Experimental and numerical investigation. *Bulletin of Volcanology*, 58(1), 19–32. <https://doi.org/10.1007/s004450050122>

- Lyakhovskiy, V., & Ilchev, A., & Agnon. (2001). Modeling of damage and instabilities of rock mass by means of a non-linear rheological model. In G. Van Aswegen, R. J. Durrheim, & W. D. Ortlepp (Eds.), *Dynamic rock mass response to mining* (pp. 413–420). South African Institute of Mining and Metallurgy.
- Lyakhovskiy, V., Melnik, O., & Shapiro, N. (2024). Modeling seismic radiation of degassing basaltic sills [Software]. *Zenodo*. <https://doi.org/10.5281/zenodo.10409298>
- Maeda, Y., & Kumagai, H. (2017). A generalized equation for the resonance frequencies of a fluid-filled crack. *Geophysical Journal International*, 209(1), 192–201. <https://doi.org/10.1093/gji/ggx019>
- Melnik, O., Lyakhovskiy, V., Shapiro, N., Galina, N., & Bergal-Kuvikas, O. (2020). Deep long period volcanic earthquakes generated by degassing of volatile-rich basaltic magmas. *Nature Communications*, 11(1), 3918. <https://doi.org/10.1038/s41467-020-17759-4>
- Melnik, O. E., Utkin, I. S., & Bindeman, I. N. (2021). Magma chamber formation by dike accretion and crustal melting: 2d thermo-compositional model with emphasis on eruptions and implication for zircon records. *Journal of Geophysical Research: Solid Earth*, 126(12), e2021JB023008. <https://doi.org/10.1029/2021JB023008>
- Mironov, N., & Portnyagin, M. (2011). H<sub>2</sub>O and CO<sub>2</sub> in parental magmas of Kliuchevskoi volcano inferred from study of melt and fluid inclusions in olivine. *Russian Geology and Geophysics*, 52(11), 1353–1367. (Melts and Fluids in Natural Mineral and Ore Formation Processes: Modern Studies of Fluid and Melt Inclusions in Minerals). <https://doi.org/10.1016/j.rgg.2011.10.007>
- Nakamichi, H., Hamaguchi, H., Tanaka, S., Ueki, S., Nishimura, T., & Hasegawa, A. (2003). Source mechanisms of deep and intermediate-depth low-frequency earthquakes beneath Iwate volcano, northeastern Japan. *Geophysical Journal International*, 154(3), 811–828. <https://doi.org/10.1046/j.1365-246X.2003.01991.x>
- Nichols, M., Malone, S., Moran, S., Thelen, W., & Vidale, J. (2011). Deep long-period earthquakes beneath Washington and Oregon volcanoes. *Journal of Volcanology and Geothermal Research*, 200(3), 116–128. <https://doi.org/10.1016/j.jvolgeores.2010.12.005>
- Nishimura, T. (2004). Pressure recovery in magma due to bubble growth. *Geophysical Research Letters*, 31(12). <https://doi.org/10.1029/2004GL019810>
- Papale, P. (1999). Modeling of the solubility of a two-component H<sub>2</sub>O + CO<sub>2</sub> fluid in silicate liquids. *American Mineralogist*, 84(4), 477–492. <https://doi.org/10.2138/am-1999-0402>
- Pitt, A. M., & Hill, D. P. (1994). Long-period earthquakes in the long valley caldera region, eastern California. *Geophysical Research Letters*, 21(16), 1679–1682. <https://doi.org/10.1029/94GL01371>
- Poliakov, A. N. B., Cundall, P. A., Podladchikov, Y. Y., & Lyakhovskiy, V. A. (1993). An explicit inertial method for the simulation of viscoelastic flow: An evaluation of elastic effects on diapiric flow in two- and three-layer models. In *Flow and creep in the solar system: Observations, modeling and theory* (pp. 175–195). Springer.
- Portnyagin, M., Hoernle, K., Plechov, P., Mironov, N., & Khubunaya, S. (2007). Constraints on mantle melting and composition and nature of slab components in volcanic arcs from volatiles (H<sub>2</sub>O, S, Cl, F) and trace elements in melt inclusions from the Kamchatka Arc. *Earth and Planetary Science Letters*, 255(1), 53–69. <https://doi.org/10.1016/j.epsl.2006.12.005>
- Portnyagin, M., Mironov, N., Botcharnikov, R., Gurenko, A., Almeev, R. R., Luft, C., & Holtz, F. (2019). Dehydration of melt inclusions in olivine and implications for the origin of silica-undersaturated island-arc melts. *Earth and Planetary Science Letters*, 517, 95–105. <https://doi.org/10.1016/j.epsl.2019.04.021>
- Power, J., Stihler, S., White, R., & Moran, S. (2004). Observations of deep long-period (DLP) seismic events beneath Aleutian Arc volcanoes: 1989–2002. *Journal of Volcanology and Geothermal Research*, 138(3), 243–266. <https://doi.org/10.1016/j.jvolgeores.2004.07.005>
- Prousevitch, A., Sahagian, D., & Anderson, A. (1993). Dynamics of diffusive bubble growth in magmas: Isothermal case. *Journal of Geophysical Research*, 98(B12), 22283–22307. <https://doi.org/10.1029/93JB02027>
- Sable, J. E., Houghton, B. F., Del Carlo, P., & Coltelli, M. (2006). Changing conditions of magma ascent and fragmentation during the etna 122 bc basaltic Plinian eruption: Evidence from clast microtextures. *Journal of Volcanology and Geothermal Research*, 158(3), 333–354. <https://doi.org/10.1016/j.jvolgeores.2006.07.006>
- Scriven, L. (1959). On the dynamics of phase growth. *Chemical Engineering Science*, 10(1), 1–13. [https://doi.org/10.1016/0009-2509\(59\)80019-1](https://doi.org/10.1016/0009-2509(59)80019-1)
- Shapiro, N. M., Droznin, D. V., Droznina, S. Y., Senyukov, S. L., Gusev, A. A., & Gordeev, E. I. (2017). Deep and shallow long-period volcanic seismicity linked by fluid-pressure transfer. *Nature Geoscience*, 10(6), 442–445. <https://doi.org/10.1038/ngeo2952>
- Shapiro, N. M., Sens-Schönfelder, C., Lühr, B. G., Weber, M., Abkadyrov, I., Gordeev, E. I., et al. (2017). Understanding Kamchatka's extraordinary volcano cluster. *Eos*, 98. <https://doi.org/10.1029/2017E0071351>
- Shaw, H. R. (1972). Viscosities of magmatic silicate liquids; an empirical method of prediction. *American Journal of Science*, 272(9), 870–893. <https://doi.org/10.2475/ajs.272.9.870>
- Shea, T. (2017). Bubble nucleation in magmas: A dominantly heterogeneous process? *Journal of Volcanology and Geothermal Research*, 343, 155–170. <https://doi.org/10.1016/j.jvolgeores.2017.06.025>
- Smith, F. W., Kobayashi, A. S., & Emery, A. F. (1967). Stress intensity factors for penny-shaped cracks: Part 1—Infinite solid. *Journal of Applied Mechanics*, 34(4), 947–952. <https://doi.org/10.1115/1.3607861>
- Song, Z., Tan, Y. J., & Roman, D. C. (2023). Deep long-period earthquakes at Akutan volcano from 2005 to 2017 better track magma influxes compared to volcano-tectonic earthquakes. *Geophysical Research Letters*, 50(10), e2022GL101987. <https://doi.org/10.1029/2022GL101987>
- Soubestre, J., Seydoux, L., Shapiro, N. M., de Rosny, J., Droznin, D. V., Droznina, S. Y., et al. (2019). Depth migration of seismovolcanic tremor sources below the Klyuchevskoy volcanic group (Kamchatka) determined from a network-based analysis. *Geophysical Research Letters*, 46(14), 8018–8030. <https://doi.org/10.1029/2019GL083465>
- Sparks, R. S. J. (1978). The dynamics of bubble formation and growth in magmas: A review and analysis. *Journal of Volcanology and Geothermal Research*, 3(1–2), 1–37. [https://doi.org/10.1016/0377-0273\(78\)90002-1](https://doi.org/10.1016/0377-0273(78)90002-1)
- Ukawa, M., & Ohtake, M. (1987). A monochromatic earthquake suggesting deep-seated magmatic activity beneath the Izu-Oshima volcano, Japan. *Journal of Geophysical Research: Solid Earth*, 92(B12), 12649–12663. <https://doi.org/10.1029/JB092iB12p12649>
- Wallace, P. J., Plank, T., Edmonds, M., & Hauri, E. H. (2015). Chapter 7 - Volatiles in magmas. In H. Sigurdsson (Ed.), *The encyclopedia of volcanoes* (2nd ed., pp. 163–183). Academic Press. <https://doi.org/10.1016/B978-0-12-385938-9.00007-9>
- Wech, A. G., Thelen, W. A., & Thomas, A. M. (2020). Deep long-period earthquakes generated by second boiling beneath Mauna Kea Volcano. *Science*, 368(6492), 775–779. <https://doi.org/10.1126/science.aba4798>
- Wegler, U., & Lühr, B. G. (2001). Scattering behaviour at Merapi volcano (Java) revealed from an active seismic experiment. *Geophysical Journal International*, 145(3), 579–592. <https://doi.org/10.1046/j.1365-246x.2001.01390.x>
- White, R. A., Newhall, C. G., & Punongbayan, R. S. (1996). Precursory deep long-period earthquakes at Mount Pinatubo: Spatio-temporal link to a basalt trigger. In *Fire and mud: Eruptions and lahars of Mount Pinatubo, Philippines* (pp. 307–328).
- Wieser, P. E., Iacovino, K., Matthews, S., Moore, G., & Allison, C. M. (2022). Vesical: 2. A critical approach to volatile solubility modeling using an open-source python3 engine. *Earth and Space Science*, 9(2), e2021EA001932. <https://doi.org/10.1029/2021EA001932>